UCRL-52077

RAMAN SPECTROSCOPIC STUDIES OF ISOTOPIC DIATOMIC MOLECULES AND A TECHNIQUE FOR MEASURING STABLE ISOTOPE RATIOS USING RAMAN SCATTERING

Robert C. Harney

(Ph. D. Thesis)

May 25, 1976

Prepared for U.S. Energy Research & Development Administration under contract No. W-7405-Eng-48

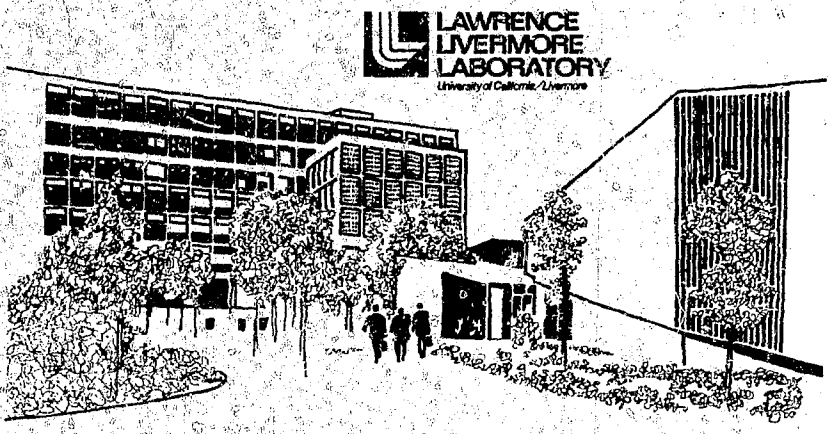

Printed in the United States of America
Available from
National Technical Information Service
U.S. Department of Commerce
5285 Port Royal Road
Springfield, VA 22161
Price: Printed Copy $; Microfiche $2.25

Page Range	Domestic Price	Page Range	Domestic Price
001–025	$ 3.50	326–350	10.00
026–050	4.00	351–375	10.50
051–075	4.50	376–400	10.75
076–100	5.00	401–425	11.00
101–125	5.25	426–450	11.75
126–150	5.50	451–475	12.00
151–175	6.00	476–500	12.50
176–200	7.50	501–525	12.75
201–225	7.75	526–550	13.00
226–250	8.00	551–575	13.50
251–275	9.00	576–600	13.75
276–300	9.25	601–up	*
301–325	9.75		

*Add $2.50 for each additional 100 page increment from 601 to 1,000 pages; add $4.50 for each additional 100 page increment over 1,000 pages.

Distribution Category
UC-34

LAWRENCE LIVERMORE LABORATORY
University of California Livermore, California 94550

UCRL-52077

RAMAN SPECTROSCOPIC STUDIES OF ISOTOPIC DIATOMIC MOLECULES AND A TECHNIQUE FOR MEASURING STABLE ISOTOPE RATIOS USING RAMAN SCATTERING

Robert C. Harney

(Ph. D. Thesis)

MS. Date: May 25, 1976

TABLE OF CONTENTS

Robert Charles Harney
May 1976
Applied Science

Raman Spectroscopic Studies of Isotopic Diatomic Molecules and
A Technique for Measuring Stable Isotope Ratios Using Raman Scattering

Abstract

A method for measuring stable isotope ratios using Raman scattering has been developed. This method consists of simultaneously counting photons scattered out of a high-intensity laser beam by different isotopically-substituted molecules. As a result of the Raman isotope effect, which causes different isotopic species to have different scattered frequencies, isolation of photons from different isotopic species is readily accomplished by using monochromators. Extrapolation of measured count rates to those obtainable by improving laser and monochromator systems to the current state-of-the-art indicates that highly-accurate isotope ratio measurements (≤0.1% precision) can be made using Raman scattering in less than one-tenth the time required for the same measurement using conventional mass spectrometry. In order to perform the necessary baseline measurements for this extrapolation a Raman spectrometer of unique capabilities was assembled. Incorporating numerous state-of-the-art components (such as 2400 g/mm holographic gratings, specially-selected RCA C31034A-02 photomultiplier tubes, and automated photon-counting data acquisition) this spectrometer can obtain much higher resolution (≈0.1 cm^{-1}) than a conventional spectrometer and allows work with signal levels heretofore impractical (<0.1 counts/sec). Using this spectrometer a number of studies of isotopic diatomic molecules have been made. The Q-branches of the Raman spectra of the isotopic molecules $^{14}N^{15}N$ and $^{16}O^{18}O$ were observed at natural abundance in nitrogen and oxygen samples. Comparison of the ratios of the intensities of the Q-branches of the major nitrogen and oxygen isotopic molecules with mass spectrometric determinations of the isotopic compositions yielded scattering cross sections of $^{14}N^{15}N$ relative to $^{14}N^{14}N$ and $^{16}O^{18}O$ relative to $^{16}O^{16}O$. These cross section ratios differ from unity, a difference which can be explained by considering nuclear mass effects on the Franck-Condon factors of the molecular transitions. The measured intensities of the $^{14}N^{15}N$ and $^{16}O^{18}O$ Q-branches

provided the baseline data needed to make the previously-mentioned extrapolation. High-resolution ($\sim$0.15 cm^{-1}) spectra of the Q-branches of $^{14}N^{14}N$ and $^{16}O^{16}O$ yielded a direct determination of α_e (the difference between the rotational constant in the ground and first excited vibrational states) for these molecules. The measured values are in excellent agreement with those obtained by other means. Complete Raman spectra (pure rotation, rotation-vibration, and high-resolution Q-branch) were obtained on a sample of pure $^{18}O^{18}O$. Analysis of this data yielded the molecular parameters: the equilibrium internuclear separation r_e, the moment of inertia I_e, and the energy parameters α_e, B_e, and $\Delta G_{1/2}$. These are in good agreement with data obtained by microwave spectroscopy.

Chapter I: Introduction

The increased availability of stable isotopes resulting from the success of the ICONS (Isotopes of Carbon, Oxygen, Nitrogen, and Sulfur) program[1-3] has caused an increase in the number and complexity of stable isotope tracer studies to the point that at some institutions (U. C. Davis among them[4]) the rate at which samples to be isotopically analyzed are being generated is exceeding the rate at which the available mass spectrometers can analyze them. As a consequence there is a growing need for improved methods of making isotope ratio determinations. This thesis describes initial work relating to the measurement of isotope ratios using laser Raman scattering, a new technique which could greatly ameliorate this situation.[5-7]

Raman scattering is the inelastic scattering of photons by atoms, molecules, or nuclei. The general physical processes are illustrated in Fig. I-1 for the specific case of vibrational scattering from molecules.[8] In Raman Stokes scattering a photon of energy $\hbar\omega_L$ scatters from a molecule in the ground state, losing energy $\hbar\omega_V$ in the process. The scattered photon carries off energy $\hbar(\omega_L-\omega_V)$ while the molecule is left in an excited vibrational state of energy $\hbar\omega_V$. In Raman anti-Stokes scattering a photon of energy $\hbar\omega_L$ scatters from a molecule in an excited state of energy $\hbar\omega_V$, gaining energy $\hbar\omega_V$ in the process. The scattered photon carries off energy $\hbar(\omega_L+\omega_V)$ leaving the molecule in its ground state. Because the scattered intensity is proportional to the number of molecules in the initial state, the ratio of anti-Stokes intensity to Stokes intensity is given roughly by the Boltzmann factor, $\exp(-\hbar\omega_V/kT)$. In the general phenomenon of Raman scattering the excited states of interest may be rotational, vibrational, electronic, or nuclear in character. However, in the remainder of this thesis we will concern ourselves primarily with Stokes vibrational scattering. A third type of scattering (not shown in Fig. I-1) is possible in which neither the photon energy nor the molecular energy are changed. This elastic scattering process is called Rayleigh scattering. Although it is usually orders of magnitude stronger than Raman scattering, it will be of minor concern in the following work.

The rate at which photons are Raman-scattered from a molecular species i is given by

$$I_{si} = \rho_i \sigma_i L I_o \qquad (I.1)$$

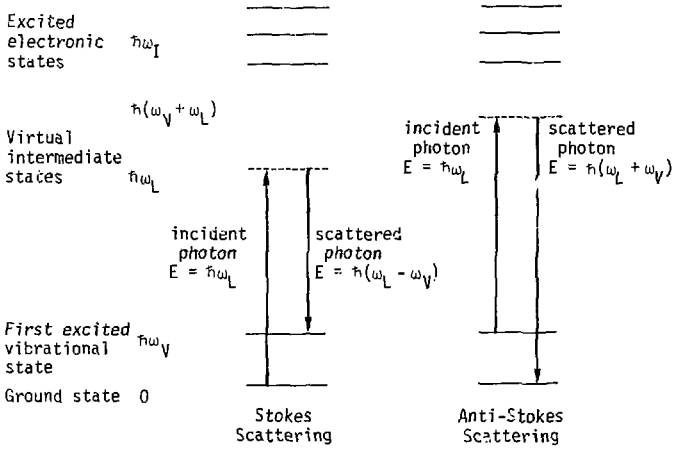

Fig. I-1. The Raman effect: Stokes and anti-Stokes scattering.

where I_0 and I_{si} are the rates (photons-sec^{-1}) at which photons are incident upon and scattered out of the scattering volume, respectively, ρ_i is the number density of species i, σ_i is the total Raman scattering cross section of species i, and L is the length of the scattering volume. Raman scattering is second order in the vector potential (one photon is absorbed and one photon is created). Consequently, the differential scattering cross section must be found using second-order perturbation theory;[9,10]

$$\frac{d\sigma}{d\Omega} = \left(\frac{e}{c}\right)^4 \omega_S \omega_L^3 \left| \sum_I \left(\frac{\langle B|\vec{r}\cdot\vec{\epsilon}_S|I\rangle\langle I|\vec{r}\cdot\vec{\epsilon}_L|A\rangle}{E_I - E_A - \hbar\omega_L - i\Gamma_I/2} + \frac{\langle B|\vec{r}\cdot\vec{\epsilon}_L|I\rangle\langle I|\vec{r}\cdot\vec{\epsilon}_S|A\rangle}{E_I - E_A + \hbar\omega_S - i\Gamma_I/2} \right) \right|^2 \quad (I.2)$$

In Eq. (I.2), e is the electron charge, c is the velocity of light, $\hbar$ is Planck's constant divided by 2π, ω_L and ω_S are the incident and scattered photon frequencies, $|A\rangle$, $|B\rangle$, and $|I\rangle$ are the wavefunctions of the initial, final, and intermediate molecular states, respectively, $e\vec{r}$ is the dipole moment operator, $\vec{\epsilon}_L$ and $\vec{\epsilon}_S$ are the polarization vectors of the incident and scattered photons, Γ_I is the width of the intermediate state I, and E_A and E_I are the energies of the initial and intermediate molecular states. It is evident from Eq. (I.2) that the scattering cross section is characteristic of each molecular species and is strongly dependent on both the incident and scattered photon energies. Table I lists the scattering cross sections for a number of simple molecules measured using photons with 488.0 nm incident wavelength.

The key to using Raman scattering for measuring isotope ratios lies in the Raman isotope effect: Molecules containing different isotopes have different scattered frequencies. The origin of this effect is the mass difference between different isotopes and is illustrated in Fig. I-2. Molecule XX has a manifold of vibrational energy levels with level separation $\hbar\omega_V \propto M^{-1/2}$ (M is the reduced molecular mass) while the isotopically-substituted molecule XX' has a manifold of vibrational energy levels with level separation $\hbar\omega_V' \propto M'^{-1/2}$. For fixed incident photon energy $\hbar\omega_L$, the scattered photon energy for molecule XX is $\hbar\omega_S = \hbar(\omega_L - \omega_V)$ while for molecule XX' it is $\hbar\omega_S' = \hbar(\omega_L - \omega_V')$. Table II compares the isotope effect in the vibrational frequencies of several simple

TABLE I

Raman Cross Sections for Selected Molecules (488.0 nm excitation).

Molecule	Raman Shift $\omega_V(cm^{-1})$	Differential Cross Section $d\sigma/d\Omega$ (cm^2-mol^{-1}-sr^{-1})	Ref.
C_6H_6	992	$3.25 \pm 0.10 \times 10^{-29}$	11
$C_6H_6CH_3$	1002	$1.83 \pm 0.06 \times 10^{-29}$	11
$C_6H_6NO_2$	1345	$1.03 \pm 0.04 \times 10^{-28}$	11
CS_2	656	$4.35 \pm 0.13 \times 10^{-29}$	11
CCl_4	459	$2.25 \pm 0.07 \times 10^{-29}$	11
N_2	2331	$3.3 \pm 1.1 \times 10^{-31}$	12
O_2	1555	$4.3 \pm 1.4 \times 10^{-31}$	12
H_2	4161	$7.9 \pm 2.6 \times 10^{-31}$	12
CO_2	1388	$4.6 \pm 1.5 \times 10^{-31}$	12
H_2O	3652	$8 \pm 3 \times 10^{-31}$	13
NH_3	3334	$1.65 \pm 0.55 \times 10^{-30}$	12
ND_3	2420	$9.9 \pm 3.3 \times 10^{-31}$	12

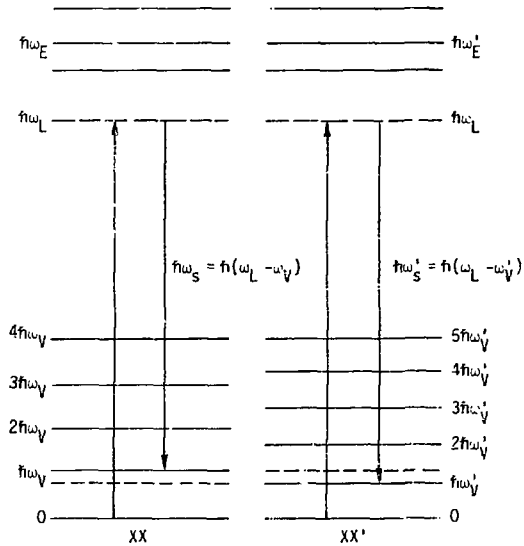

Fig. I-2. Origin of the Raman isotope effect.

TABLE II.

The Isotope Effect in Selected Molecules.

Molecule	ω_V (cm^{-1})	Ref. No.	Molecule	ω_V (cm^{-1})	Ref. No.
H_2	4161.1	14	$^{10}BF_3$	482.0	8a
HD	3632.1	14	$^{11}BF_3$	480.4	8a
D_2	2994.4	8a			
HT	3433.1	8a	$^{12}C^{16}O_2$	1388.2	16
DT	~2686.0	8a	$^{13}C^{16}O_2$	1369.9	16
T_2	2466.1	8a			
			$^{12}C^{32}S_2$	658.0	16
$^6Li_2$	~373.9	8a	$^{12}C^{32}S^{33}S$	653.0	16
$^6Li^7Li$	~360.3	8a	$^{12}C^{32}S^{34}S$	648.4	16
$^7Li_2$	346.2	8a			
			$^{12}C_6H_6$	991.6	8a
$^{14}N_2$	2330.7	8a	$^{12}C_5{}^{13}CH_6$	984	8a
$^{14}N^{15}N$	~2291.5	8a			
$^{15}N_2$	~2251.7	8a	$^{12}C_6D_6$	944.7	8a
			$^{12}C_5{}^{13}CD_6$	939.5	8a
$^{16}O_2$	1556.3	15			
$^{17}O_2$	~1509.8	15	$^{12}C^{35}Cl_4$	461.5	8a
$^{18}O_2$	~1467.3	15	$^{12}C^{35}Cl_3{}^{37}Cl$	458.4	8a
$^{16}O^{17}O$	~1533.2	15	$^{12}C^{35}Cl_2{}^{37}Cl_2$	455.1	8a
$^{16}O^{18}O$	~1512.5	15	$^{12}C^{35}Cl^{37}Cl_3$	~452.0	8a
$^{17}O^{18}O$	~1488.7	15	$^{12}C^{37}Cl_4$	~448.9	8a

~A calculated frequency.

molecules. It is important to note that in many instances the isotope shift is several cm^{-1} or larger, sufficiently large to be easily resolved by a monochromator.

Given that photons scattered from different isotopic species may be isolated and detected separately, the question arises as to what accuracies may possibly be obtained and what times would be required to obtain them. Order-of-magnitude answers to these questions can be obtained by considering an example. Table III lists the natural isotopic abundances for some selected elements. Since typical values for low-abundance isotopes are 10-0.01%, let us consider a model element consisting of two isotopes with abundances of 99.9% and 0.1%. Three diatomic species can be formed from these isotopes. For most elements the equilibrium abundances of the three diatomic species are close to those predicted by the quadratic distribution: if abundance(A)=x and abundance(B)=y, the abundance(AA)=x^2, abundance(AB)=2xy, and abundance(BB)=y^2. The quadratic distribution is the correct distribution if the formation of the diatomic molecules is controlled by kinetic processes rather than equilibrium processes. In either case for the model element the abundance of BB is so small that a 0.1% precision isotope measurement can be made by determining the abundances of AA and AB alone.

Using a modification of Eq.(I.1), the measured intensity of photons scattered from the i^{th} species is given by

$$I_{mi} = \varepsilon_i \rho_i \sigma_i L I_o \qquad (I.3)$$

where ε_i is the combined collection-detection efficiency for photons scattered from the i^{th} species. Using typical values of $\varepsilon_{Ai} \sim 10^{-4}$, $\rho_{AA} \sim 2.7 \times 10^{19}$ cm^{-3} (STP), $\sigma_{AA} \sim 10^{-29}$ cm^2, L ~1 cm, and $I_o \sim 3 \times 10^{19}$ photons-sec^{-1} (10 W at 488.0 nm), the measured intensity for species AA is approximately

$$I_{mAA} \sim 8 \times 10^5 \text{ photons-sec}^{-1}.$$

For the species AB (2xy=0.002)

$$I_{mAB} \sim 1600 \text{ photons-sec}^{-1}.$$

Since Raman scattering is a random process, the Raman-scattered photons obey Poisson statistics. Consequently, if N counts are obtained from a given isotopic species the uncertainty in this value is of the order of

TABLE III.

Natural Isotopic Abundances of Selected Elements.

Element	Isotope	Abundance (%)	Element	Isotope	Abundance (%)
Hydrogen	^{1}H	99.985	Chlorine	^{45}Cl	75.77
	^{2}H	0.015		^{37}Cl	24.23
	^{3}H	-	Potassium	^{39}K	93.08
Lithium	^{6}Li	7.56		^{40}K	0.0118
	^{7}Li	92.44		^{41}K	6.91
Boron	^{10}B	19.8	Iron	^{54}Fe	5.8
	^{11}B	80.2		^{56}Fe	9 .7
Carbon	^{12}C	98.89		^{57}Fe	2.14
	^{13}C	1.11		^{58}Fe	0.31
	^{14}C	-	Rubidium	^{85}Rb	72.15
Nitrogen	^{14}N	99.63		^{87}Rb	27.85
	^{15}N	0.37	Mercury	^{196}Hg	0.146
Oxygen	^{16}O	99.759		^{198}Hg	10.02
	^{17}O	0.037		^{199}Hg	16.84
	^{18}O	0.204		^{200}Hg	23.13
Silicon	^{28}Si	92.21		^{201}Hg	13.22
	^{29}Si	4.70		^{202}Hg	29.80
	^{30}Si	3.09		^{204}Hg	6.85
Sulfur	^{32}S	95.00	Uranium	^{234}U	0.0057
	^{33}S	0.76		^{235}U	0.72
	^{34}S	4.22		^{238}U	99.27
	^{36}S	0.014			

$N^{1/2}$. Thus, to make a 0.1% precision isotope ratio measurement, 10^6 counts must be obtained on the low-abundance species. In the example this would take 600 sec or 10 min, which is comparable to or better than the performance of a mass spectrometer in making the same measurement.

This result indicates that Raman scattering may have a potentially great impact on the measurement of stable isotope ratios. However, in the preceding example a number of assumptions concerning the isolatability of the different isotopic lines, the efficiency of the detectors, etc., had to be made. Consequently, a good deal of experimental work must be done to determine the validity of these assumptions.

One possible complication in isolating the different isotopic vibrational lines may arise from the rotational structure of these lines. Fig. I-3 shows the theoretical Raman spectrum of a model diatomic molecule. Three branches or groups of rotation-vibration lines are evident. These are the Q-branch in which the rotational quantum number J does not change ($\Delta J=0$), the S-branch in which the rotational quantum number increases by two ($\Delta J=+2$), and the O-branch in which the rotational quantum number decreases by two ($\Delta J=-2$). The vibrational quantum number v increases by one ($\Delta v=+1$) in all three branches. Each line in each branch corresponds to a different rotational quantum number. The intensity of each line is proportional to the product of its degeneracy and its Boltzmann factor. Shown superimposed on this spectrum is the Q-branch of another isotopic species of lower abundance. As shown, the majority of the intensity in the low-abundance isotopic Q-branch can be integrated without obtaining any contribution from the adjacent O-branch lines of the high-abundance species. However, if the position of this Q-branch were shifted slightly, only a fraction of the intensity could be integrated without interference. Such interference could significantly impair the accuracy of the isotope ratio measurements.

To determine whether interference such as that mentioned above is indeed a problem it is necessary to obtain high-quality Raman spectra of the isotopic species of interest. To accomplish this a state-of-the-art Raman spectrometer was constructed. Several recent developments such as holographic diffraction gratings[17] which eliminate grating ghosts and significantly reduce stray light in the monochromator and

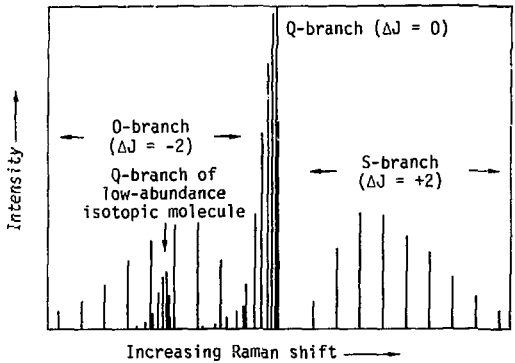

Fig. I-3. Theoretical Raman spectrum of a diatomic molecule showing isotope structure.

a new type of photomultiplier tube with high quantum efficiency and exceptionally low dark noise were incorporated into this spectrometer to increase its performance to the maximum attainable. Similarly, to accomodate the exceedingly long integration times required in this work, true photon-counting detection was utilized and an automated data acquisition system was developed. Complete details of the construction and operation of this spectrometer system are contained in Chapter II of this thesis.

A number of studies of isotopic molecules of nitrogen and oxygen were performed using this spectrometer. First, the isotope structure of nitrogen and oxygen was investigated. Medium-resolution spectra showed that $^{14}N^{14}N$ did not interfere with $^{14}N^{15}N$, $^{16}O^{16}O$ did not interfere with $^{16}O^{18}O$ or $^{18}O^{18}O$, and $^{18}O^{18}O$ did not interfere with $^{16}O^{16}O$. Unfortunately $^{16}O^{16}O$ was found to interfere with $^{16}O^{17}O$. Next, the relative scattering cross sections of $^{14}N^{15}N$ and $^{16}O^{18}O$ were measured. In addition to yielded some very interesting physical results, this exercise yielded data on absolute count rates in a realistic situation. Because of the success in obtaining high-quality Raman spectra in poor signal-to-noise situations it was decided to obtain high-resolution spectra of the Q-branches of $^{16}O^{16}O$, $^{14}N^{14}N$, and $^{18}O^{18}O$. In each of these spectra a number of rotational lines were resolved, the frequencies of which were used to obtain direct measurements of the rotation-vibration coupling constants of these molecules. Finally, complete rotational and rotation-vibration Raman spectra were obtained of an $^{18}O^{18}O$. These previously-unmeasured spectra yielded the molecular parameters of this molecule. A discussion of these various studies comprises Chapter III of this thesis.

Chapter IV discusses the use of Raman scattering for measuring isotope ratios. First, expressions are obtained for determining the isotope ratios and isotopic abundances from intensity measurements of any complete set of isotopic molecules. Next, a specific isotope ratio spectrometer system is presented and its performance is analyzed in terms of the baseline data presented in Chapter III. Finally, several additional Raman-scattering isotope ratio measurement systems are discussed in this same context.

The results of the preceding chapters are summarized in Chapter V. Special attention is given to the probable advantages and disadvantages of the Raman scattering technique. For measuring certain important isotope ratios, such as $^{1}H/^{2}H$, $^{14}N/^{15}N$, and $^{16}O/^{18}O$, it appears that the Raman scattering approach can be far superior to mass spectrometry. For measuring certain other ratios, such as $^{3}He/^{4}He$, it will be totally inadequate. Finally, a brief discussion of unanswered questions and areas for further research is presented.

Chapter II: An Automated, Photon-Counting Raman Spectrometer

To obtain the data needed to verify the suitability of Raman scattering as a technique for measuring stable isotope ratios, it was necessary to assemble a Raman spectrometer whose capabilities far exceeded those of conventional Raman spectrometers. To accomplish this it was necessary to carefully consider almost every aspect of spectrometer design. There are three main processes involved in Raman spectroscopy: production of the scattered signal, wavelength analysis of this scattered signal, and detection and recording of this spectral signal. We consider this last aspect first.

There are four general techniques applicable for signal detection in uv-visible spectroscopy: photographic, photoelectric, count-rate, and photon-counting. These are illustrated schematically in Fig. II-1. In photographic recording the spectral signal (from a monochromator or spectrograph) is imaged onto a photographic plate.[18] This plate is developed and the grain density as a function of position is determined using a microdensitometer and recorded on a chart recorder or similar device. The characteristics of this technique are the requirement of strong signals ($>10^6$ photons per resolution element), analog output (unless an analog-to-digital converter is used), and an uncertainty in the measured intensities which cannot be quantitatively determined solely from examination of the experimental data. That is, the intensity uncertainty is not determined by the photon statistics of the data. Noise and systematic errors can enter the data through irregularities in the photographic emulsion, reciprocity failure and D-logE nonlinearity of the film, noise in the microdensitometer, and the presence of background or spurious signals (fluorescence, stray scattered light, etc.).

In photoelectric recording the spectral signal is incident

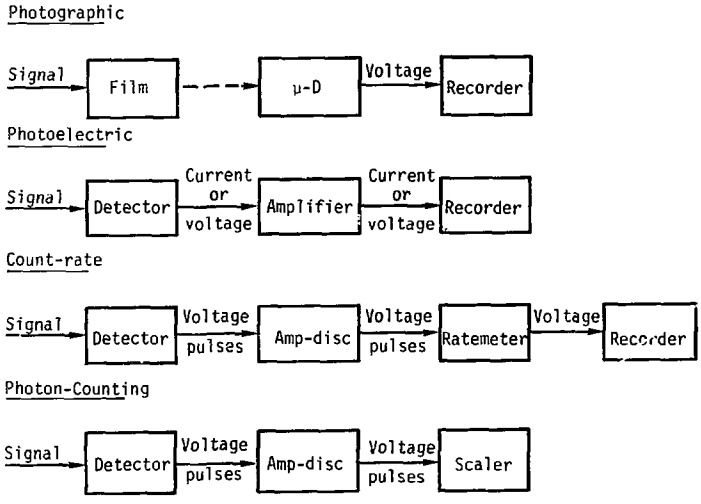

Fig. II-1. Schematic representation of the four principal techniques for signal detection and recording in uv-visible spectroscopy.

upon a photoelectric or photovoltaic device which generates either an analog current or voltage signal. This signal is amplified and recorded on a chart recorder. This technique has the characteristics of requiring a strong signal ($>10^3$ photons/sec), yielding an analog output, and having a nonquantitative intensity uncertainty. Noise sources are the amplifier and recorder, thermal noise (dark current) in the photodetector, and background signals.

An improvement on the standard photoelectric technique is count-rate recording. The spectral signal is incident upon a detector which emits voltage pulses when struck by invididual photons. These pulses are amplified (and possibly discriminated in intensity), integrated by a ratemeter, and the resulting analog signal recorded on a chart recorder. The characteristics of this technique are the ability to handle moderately weak signals (>10 photons/sec), analog output, and a semi-quantitative uncertainty in intensity. Noise sources are thermal noise, quantum noise (resulting from the fact that Raman-scattered photons obey Poisson statistics; see Table IV), recorder noise, and background signals.

In true photon-counting, the spectral signals generate voltage pulses in a photomultiplier which are amplified and discriminated in intensity (to remove some of the thermal noise). These pulses are then counted directly with a scaler. The characteristics of this technique are the ability to handle extremely weak signals (the minimum detectable signal is limited only by the time available for integration and the noise level; 0.1 photon/sec is readily detected if the noise is less than 10 counts/sec and a 1000 sec integration time is used), direct digital output, and a quantitative intensity uncertainty (this is the result of the lack of non-Poisson noise sources). Noise sources are restricted to thermal noise, quantum noise, and background signals.

The characteristics of all of the above detection methods are

TABLE IV

Brief Summary of Poisson Statistics

Probability distribution function

$$P(n) = \exp(-\bar{n})\ \bar{n}^n/n!$$

n = measured number of counts per unit time

$\bar{n}$ = average number of counts per unit time

Signal-to-noise ratio for no outside noise sources

$$S/N = n^{1/2}$$

Signal-to-noise ratio for constant background noise n_B

$$S/N = n/(n + n_B)^{1/2}$$

Signal-to-noise ratio for proportional background noise $n_p = \alpha n$

$$S/N = n/(n + n_p)^{1/2} = (n/(1 + \alpha))^{1/2}$$

summarized in Table V. Inspection of this table indicates that photon-counting is a superior technique in almost all respects. In addition, the Poisson nature of the data means that the signal-to-noise ratio can be improved almost without limit if enough counts can be obtained. In the count-rate technique integration times are limited to approx. 30 sec or less, whereas in the photon-counting technique integration times can be made to exceed 3600 sec per data point with a substantial resulting increase in signal-to-noise ratio. As a result photon-counting detection was an obvious choice for studies of isotopic molecules in the gas phase. However, in some spectral studies it is desirable to see the spectrum in real time. With photon-counting detection rather sophisticated electronics (such as an on-line minicomputer) are required to allow this, although with count-rate detection a chart recorder will suffice. Consequently, it was decided to design the spectrometer with the option of simultaneous photon-counting and count-rate detection.

Since Raman scattering is an extremely weak process and must compete with stronger processes, such as Rayleigh scattering and fluorescence, it is extremely important to pay careful attention to maximizing the efficiency of the wavelength analyzer and detector and minimizing all possible sources of noise. One major source of noise is stray scattered light in the wavelength analyzer. Almost all wavelength analysis in Raman spectroscopy is performed by diffraction grating monochromators or spectrographs, and although all optical surfaces will scatter some light in all directions due to microscopic imperfections, diffraction gratings are notoriously bad. The extremely strong Rayleigh and fluorescence signals can scatter from the mirrors and gratings in a monochromator or spectrograph and cause signals at the detector even though the monochromator is detuned from the Rayleigh or fluorescent wavelengths.

TABLE V

Characteristics of uv-visible Spectral Recording Techniques

Photographic

Strong signal required

Analog output

Noise sources - emulsion irregularities, background light, microdensitometer noise, reciprocity failure, and D-logE nonlinearity

Intensity uncertainty is non-quantitative

Photoelectric

Strong signal required

Analog output

Noise sources - thermal noise, background light, amplifier noise, recorder noise

Intensity uncertainty is non-quantitative

Count-rate

Weaker signal allowed

Analog output

Noise sources - quantum noise, thermal noise, background light, recorder noise

Intensity uncertainty is semi-quantitative

Photon-counting

Very weak signal allowed

Digital output

Noise sources - quantum noise, thermal noise, background light

Intensity uncertainty is quantitative

In addition small errors in the rulings of the diffraction gratings result in grating ghosts, or weak lines appearing as satellites to very strong spectral lines.[19]

If single-channel detection (i.e. a photomultiplier tube) is used, much of the problem of stray light and grating ghosts can be eliminated by using a double monochromator. The first monochromator of a double monochromator serves to reject all of the incident light except that which is scattered in a direction corresponding to a narrow wavelength region of interest. The second monochromator then reanalyzes this transmitted light. Because the total intensity incident on the entrance slit of the second monochromator (which is also the exit slit of the first monochromator in most commercial instruments) is drastically reduced, the stray light problem is correspondingly reduced. Unfortunately, the second monochromator also reduces the overall efficiency of the system.

However, stray light problems still exist when attempting to obtain Raman spectral data close to a strong line (such as the Rayleigh line). Methods for further reducing the stray light problem include narrow-band filtration of the unwanted light (e.g. use of an I_2 vapor filter to reduce the Rayleigh scattering of 514.5 nm laser radiation) or addition of a third monochromator. Both of these methods complicate the operation of the wavelength analyzer and reduce its efficiency. Recently, however, a breakthrough has been made in grating technology. Holographically-ruled diffraction gratings can now be fabricated with no ruling errors and a minimum of imperfections.[14] As a result ghosts can be eliminated and stray light scattering reduced orders-of-magnitude by using these gratings, with only about a 50% reduction in efficiency when compared to classically-ruled gratings. For our Raman spectrometer,

a SPEX Model 1402 double monochromator with 2400 groove/mm holographic gratings was chosen for wavelength analysis.[20] The choice of 2400 groove/mm gratings instead of the standard 1800 groove/mm gratings was made to obtain increased resolution and efficiency.

Another major source of noise is dark noise in the detector. Even a reasonably small amount of dark noise can completely mask the weak Raman-scattered signals from gases. Traditionally, photodetectors with low dark noise have had low quantum efficiencies. However, a recent development is photomultiplier tubes with GaAs reflection photocathodes. One such tube, the C31034A-02 photomultiplier from RCA has a typical quantum efficiency of 30% for visible photons and less than 4 dark counts/sec when cooled to -70°C, which is adequate for most of our purposes.

A final consideration concerns production of the scattered signal. The data acquisition rates for signals which are comparable to or greater than the noise and photon-counting detection is maximized when the scattered signal is cw. For signals much weaker than the noise a pulsed source with synchronous gated detection maximizes the signal-to-noise. In the situations envisioned in isotope studies the cw case is optimum. In most materials the scattered signal increases as the incident photon flux increases (materials which photodecompose being the exception) and as the frequency of the incident photons increases. Consequently visible ion lasers prove to be the best choice for an excitation source although dye lasers and gas mixture lasers often suffice. The optical power inside the cavity of a laser is substantially higher than the power in an external beam and some groups working with gases have placed their scattering cells inside the laser cavity to take advantage of this fact. However, this requires specially-designed scattering cells and constant attention because small misalignments in the cell position or improper cleaning can

dramatically reduce the laser power. Because we wanted to have the capability of handling solids and liquids as well as gases we opted to use cells positioned in an external beam.

The spectrometer which resulted from consideration of all of the above is shown schematically in Fig. II-2 and pictorially in Fig. II-3.[21,22] Two lasers are available as excitation sources: a Spectra-Physics model 125 helium-neon laser (80 mW at 632.8 nm wavelength) or a Spectra-Physics model 165 argon ion laser (1.0 W at either 488.0 or 514.5 nm wavelength). The output beam from the appropriate laser (the choice depends on the sample being studied) is passed through a narrow-band interference filter to remove non-lasing lines emanating from the plasma in the laser discharge tube, polarized by a Glan-Thompson prism, and focused into the appropriate sample cell. A portion of the laser beam is split off from the main beam and directed onto an RCA 8575 photomultiplier (PM) tube. The output from this photomultiplier tube is used as a monitor on the laser output power. Fig. II-4 shows the arrangement of the Ar^+ laser, the monitor PM tube, and the miscellaneous optics.

To handle the wide variety of samples envisioned in the isotope studies and other studies of interest to us a number of sample cells and cell holders had to be fabricated. All of these were designed to be compatible with the standard SPEX 1430 sample illumination chamber. Fig. II-5 shows the laser beam passing through a SPEX 1435 50 µl. liquid cell placed in a temperature-controlled holder. The light-collecting lens is shown in the background. This temperature-controlled holder (which can also be used with horizontally-mounted 1 mm OD capillary cells) is shown in detail in Fig. II-6. The large steel heat sink contains coolant coils and is connected through insulated tubing to a glycol heater-chiller unit. A thermistor embedded in the heat sink provides a feedback loop for

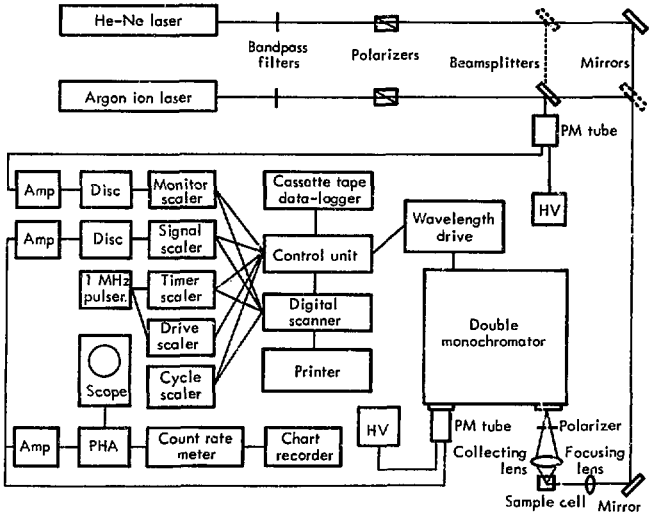

Fig. II-2. Schematic diagram of the photon-counting Raman spectrometer and automated data acquisition system.

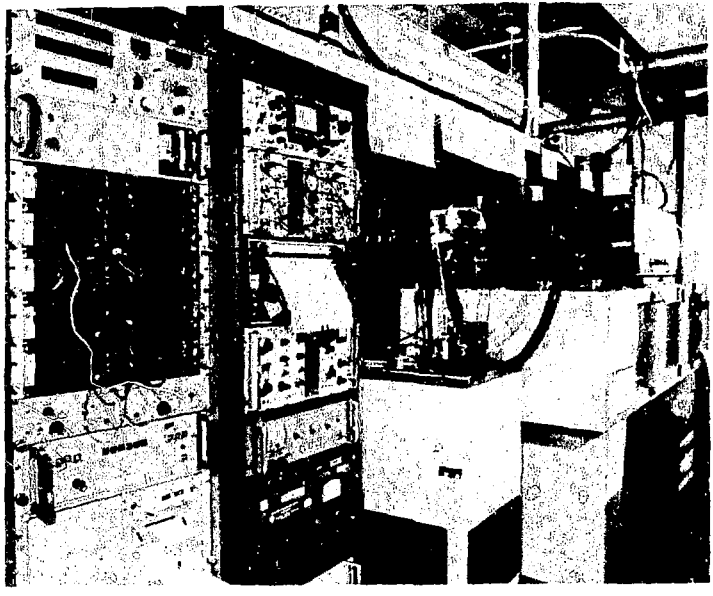

Fig. II-3. Overall view of the photon-counting Raman spectrometer and data acquisition system.

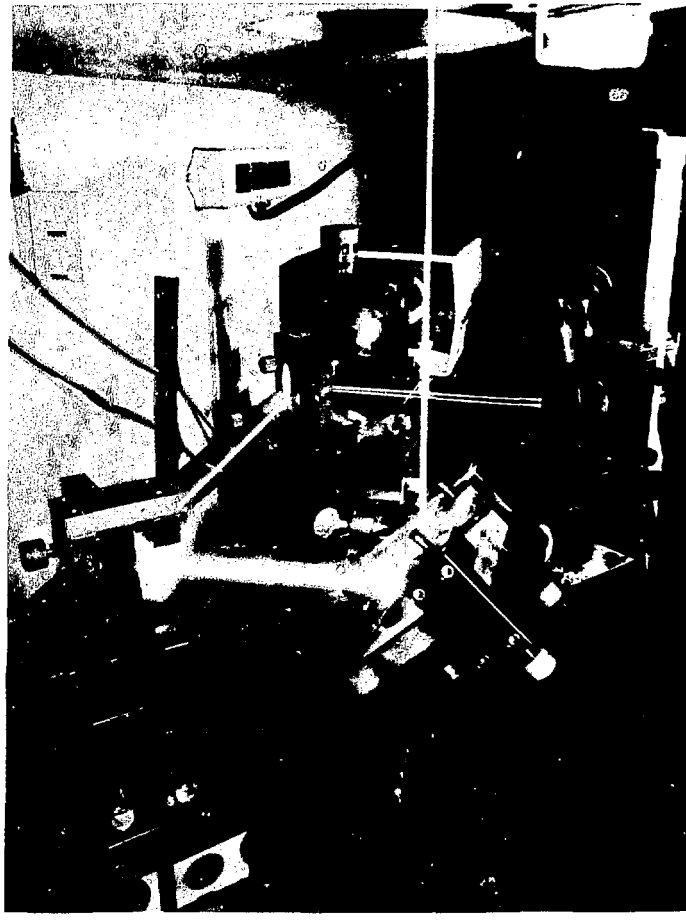

Fig. II-4. Photograph of the argon ion laser, monitor photomultiplier tube, and miscellaneous optics.

Fig. II-5. Photograph of the focused laser beam passing through a 50μl liquid cell placed in the temperature-controlled holder.

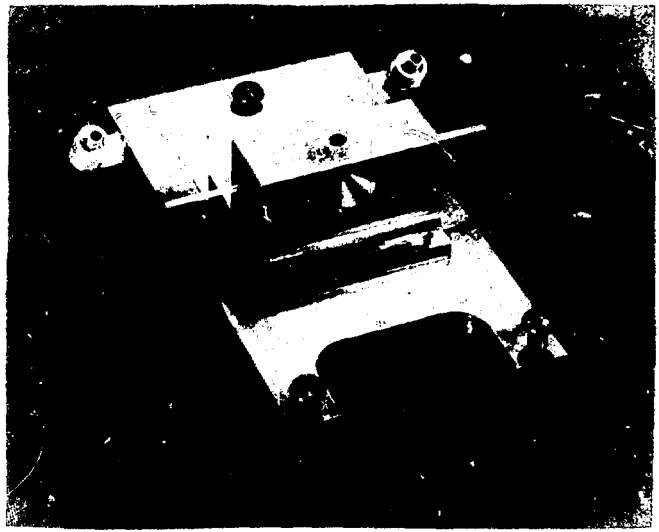

Fig. II-6. Photograph of the temperature-controlled holder (removed from the spectrometer) with a capillary tube cell in place.

temperature stability. Using this unit the sample temperature can be controlled to ± 0.1°C over the range -20°C to + 80°C. When operating at low temperatures, the illumination chamber is purged with dry nitrogen to prevent condensation. Fig. II-7 shows a scattering cell for gases and its holder. The cell is constructed by attaching an 18/9 ground glass joint and a vacuum stopcock to a type 63 fused silica cell from Precision Cells. The cell is held in place in an aluminum block by six nylon screws adjusted to be under slight compression when the cell is inserted. This arrangement allows the cell to be repeatably positioned in the laser beam. A Waters sample holder for powdered samples is also available.[23]

Photons scattered from any of the above sample cells are collected by a 17 mm, f/0.95 lens, passed through a polarization analyzer and a polarization scrambler, and imaged onto the entrance slit of the SPEX 1402, f/6.9, 0.75-meter double monochromator equipped with 2400 groove/mm holographic gratings. Detection of the photons which are passed by the monochromator is accomplished with an RCA C31034A-02 PM tube cooled to -70°C by a Products for Research thermoelectric cryostat using chilled (-30°C) methanol for heat exchange. The output pulses from both PM tubes (signal and monitor) are amplified by ORTEC 9301 fast preamplifiers and LRS 133B dual linear amplifiers, discriminated by LRS 123 threshold discriminators and recorded on Livermore LE8400 twelve-decade scalers. The output of the signal discriminator is also connected to an ORTEC 449 log/lin ratemeter and a Hewlett-Packard 7101B electrostatic chart recorder. A Tektronix R647A oscilloscope is available for pulse diagnostics.

Acquisitic of the photon-counting data is facilitated by a microcomputer control unit. Connected to this unit are the signal and monitor scalers, three additional scalers (two connected to a 1 MHz pulser which serve as timers for the count time and

Fig. II-7. Photograph of the gas-phase scattering cell and its special holder (with a second cell in place).

wavelength drive time, and one which records the number of data collection cycles which have been completed), a Dymec six-channel digital scanner and line printer, and a Datel Systems LPS-16 cassette tape data-logger. A number of presets on the control unit control the taking and recording of photon-counting spectra in the following manner. Counts are obtained on the signal and monitor scalers for a preset time and/or a preset number of counts on either scaler (any desired logical combination of "and" and "or" is permissible using the presets). The cycle scaler is advanced one and the data (signal counts, monitor counts, count time, and cycle number) are recorded on both the scanner-line printer system and the data-logger. The data scalers are then reset, and the wavelength drive is activated for a preset time corresponding to a small predetermined wavelength increment. This increment may be as small as 0.02 cm^{-1} (limited by mechanical stability of the wavelength drive). This sequence is repeated until the desired number of data points is obtained.

Graphical representation of the resulting spectrum may be obtained either by plotting the line printer data by hand or by plotting the data-logger data on a Hewlett-Packard 9860 plotter connected to a Hewlett-Packard 9830 calculator. A computer program written for this system allows a number of data reduction techniques to be applied to the data-logger data. In addition to ordinary plotting, the signal can be normalized to the number of monitor counts, the count time, or both, one-standard-deviation error bars can be calculated and plotted, and the data can be smoothed using a three-point average before plotting.

Chapter III: Studies of Isotopic Nitrogen and Oxygen Molecules

Using the Raman spectrometer described in the previous chapter a number of studies were initiated which were aimed at establishing the feasibility of measuring stable isotope ratios using Raman scattering. First and foremost among these were studies of the isotope structure of nitrogen and oxygen, the purpose of which was to demonstrate that, at least in some cases of interest, the rotational structure of one isotopic species does not interfere with the Q-branches of the other isotopic species of interest. Oxygen and nitrogen were singled out for these initial studies because of their simplicity and the extreme utility of $^{14}N/^{15}N$ and $^{16}O/^{18}O$ isotope ratios in tracer studies.

To determine the wavelength regions of interest count-rate spectra were obtained (1.3 cm^{-1} resolution, 30 sec integration time, and 1.0 W laser power at 488.0 nm) of the entire rotation-vibration spectra of samples of nitrogen in air (Fig. III-1) and oxygen (Fig. III-2) gas at atmospheric pressure. In each of these spectra there is evidence for the presence of the Q-branch of the low-abundance isotopic species between two lines of the O-branch of the high-abundance species. Next, photon-counting spectra were obtained in the vicinities of the Q-branches of these low-abundance isotopic species. In Fig. III-3 the Q-branch of $^{14}N^{15}N$ is shown clearly resolved between the J=6 → J=4 and J=5 → J=3 lines of $^{14}N^{14}N$, while in Fig. III-4 the Q-branch of $^{16}O^{18}O$ is also shown clearly resolved between the J=9 → J=7 and J=7 → J=5 lines of $^{16}O^{16}O$. In each case the Q-branch was identified by its appearance at the predicted wavelength and by its characteristic asymmetric shape. The rotational lines were identified by comparison with the count-rate spectra taking the effects of nuclear spin on the line intensities (^{14}N is a spin one nucleus and $^{14}N^{14}N$ has a singlet

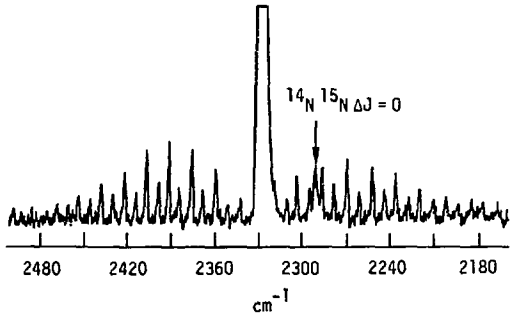

Fig. III-1. The rotation-vibration Raman spectrum of nitrogen in air.

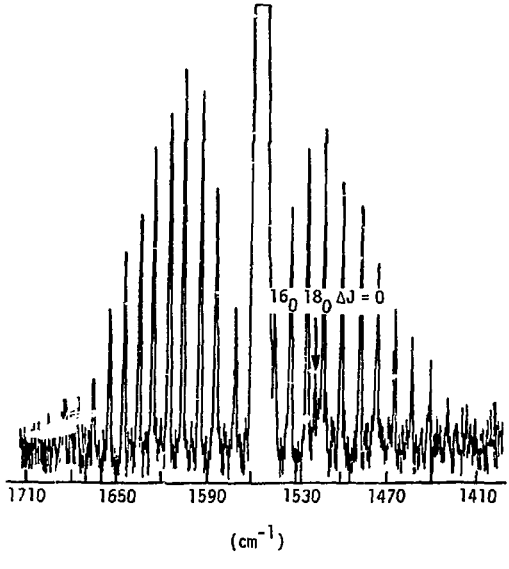

Fig. III-2. The rotation-vibration Raman spectrum of oxygen gas.

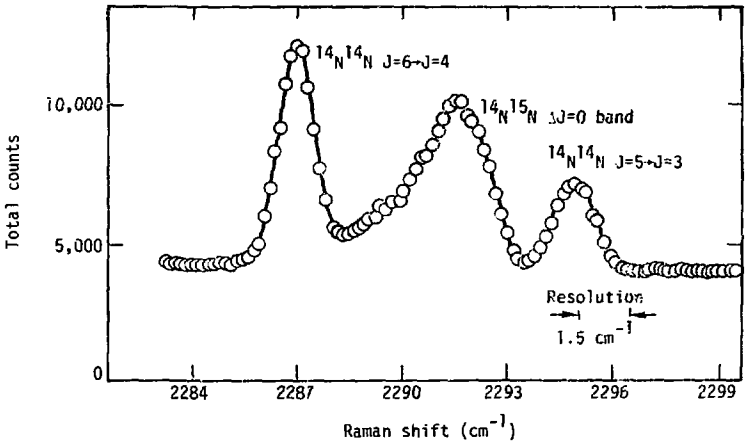

Fig. III-3. Medium-resolution spectrum of the Q-branch of $^{14}N^{15}N$ in air.

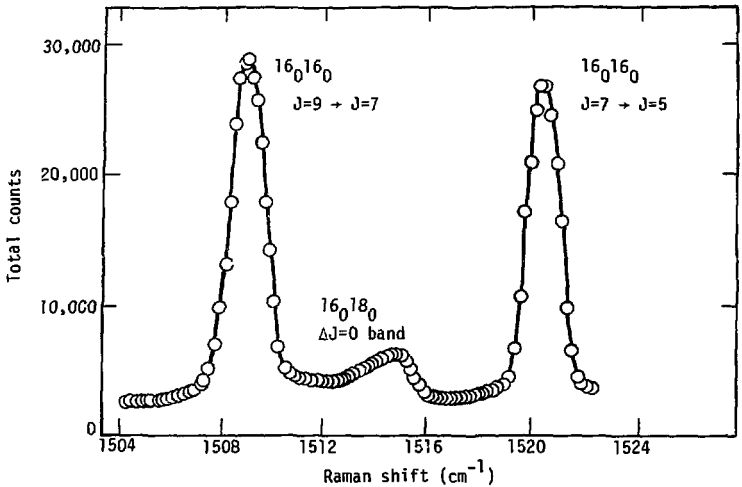

Fig. III-4. *Medium-resolution spectrum of the Q-branch of* $^{16}O^{18}O$ in oxygen gas.

ground electronic state, therefore nuclear statistics predicts an alteration in intensity of J(odd):J(even) = 1:2 for $^{14}N^{14}N$; ^{16}O is a spin zero nucleus and $^{16}O^{16}O$ has a triplet ground electronic state, therefore statistics predicts that only odd J rotational levels are allowed) into consideration. For both spectra the resolution was 1.5 cm^{-1}, the spacing between data points was 0.15 cm^{-1}, and the integration time was 1000 seconds per data point.

Prompted by the quality of the preceding spectra and the comments of others we investigated other aspects of the isotope structure of nitrogen and oxygen. The Raman spectrum of the Q-branch of $^{16}O^{17}O$ in natural abundance oxygen gas is shown in Fig. III-5. The resolution was 1.0 cm^{-1}, data point spacing was 0.3 cm^{-1}, the laser power was 900 mW at 488.0 nm, and the integration time was 3600 seconds per point. In this case the J=5 → J=3 line of $^{16}O^{16}O$ lies right on top of the $^{16}O^{17}O$ Q-branch. Figs. III-6 and III-7 show the Q-branch of a 5% $^{18}O^{18}O$ impurity in $^{16}O^{16}O$ gas and the Q-branch of a 2% $^{16}O^{16}O$ impurity in $^{18}O^{18}O$ gas, respectively. For both spectra the resolution was 1.0 cm^{-1}, the data point spacing was 0.3 cm^{-1}, the laser power was 700 mW at 488.0 nm, and the integration time was 600 seconds per point. The Q-branch of $^{18}O^{18}O$ is clearly resolved between the J=17 → J=15 and J=15 → J=13 lines of $^{16}O^{16}O$ while the Q-branch of $^{16}O^{16}O$ is clearly resolved between the J=15 → J=17 and J=17 → J=19 lines of $^{18}O^{18}O$.

Examination of Figs. III-3 through III-7 indicates that approximately 95% of the intensity of any of the isotopic Q-branches falls in a wavelength region 4 or 5 cm^{-1} wide, which is narrower than the spacing between the $\Delta J=\pm 2$ lines in their vicinity. As a result, it should be possible to integrate completely some of the isotopic Q-branches without obtaining significant contributions from the adjacent rotational structure

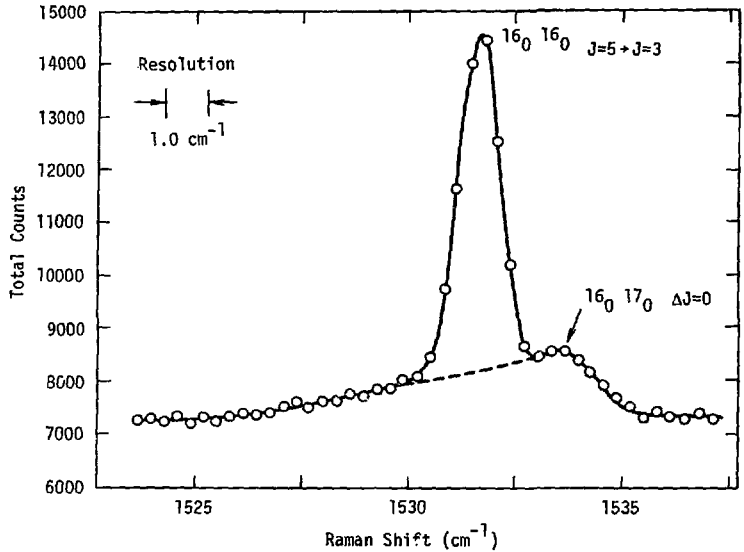

Fig. III-5. Raman spectrum of natural oxygen gas showing the Q-branch of $^{16}_{0}{}^{17}_{0}$.

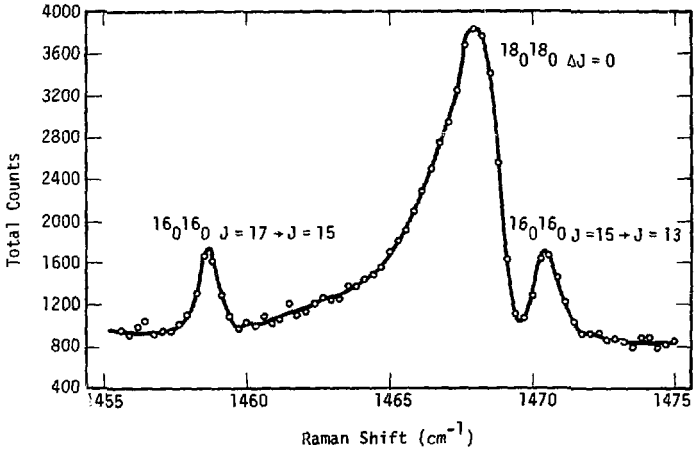

Fig. III-6. Raman spectrum of $^{16}O^{16}O$ gas showing the Q-branch of an $^{18}O^{18}O$ impurity.

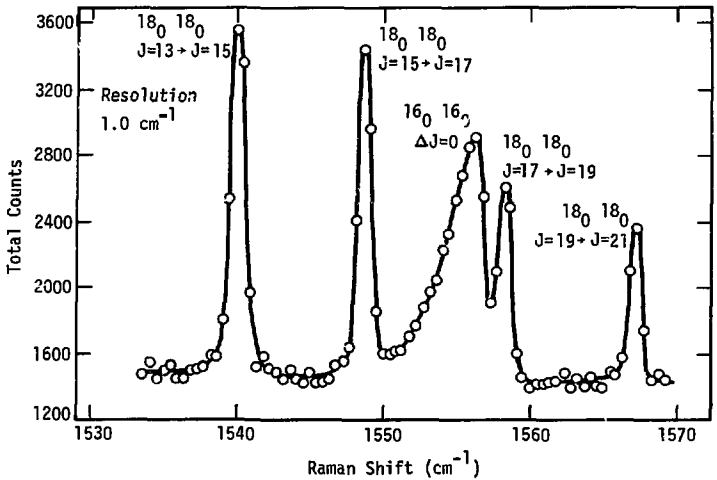

Fig. III-7. Raman spectrum of $^{18}O^{18}O$ gas showing the Q-branch of an $^{16}O^{16}O$ impurity.

of other isotopic species. This suggests the possibility of measuring the relative Q-branch Raman scattering cross sections of the various isotopic molecules.

The relative cross sections of $^{14}N^{15}N$ and $^{14}N^{14}N$ were determined in the following manner. Scans of 4 cm^{-1} resolution, 1000 sec/pt. and 0.2 cm^{-1} data point spacing were obtained at the peaks of the Q-branches of both $^{14}N^{14}N$ and $^{14}N^{15}N$ on a sample of air at 1 atm and 24°C using a laser power of 1.3 W at 488.0 nm. After normalizing the data to the same total laser fluence and correcting for the wavelength-dependent spectrometer efficiency (determined by obtaining the spectrum of an NBS standard source) the peak count rates of these scans yielded the relative scattered intensities, $I_{14\text{-}15}/I_{14\text{-}14} = 0.0081 \pm 0.0002$. The 3% uncertainty is due primarily to uncertainties in the wavelength-dependent spectrometer efficiency calibration and the lack of 100% Q-branch integration and not to photon statistics (<1%). The ratio of the number density of $^{14}N^{15}N$ molecules to the number density of $^{14}N^{14}N$ molecules was obtained by analyzing the sample with a conventional mass spectrometer.[24] This analysis yielded $N_{14\text{-}15}/N_{14\text{-}14} = 0.0072 \pm 0.0001$. Since the scattered intensity is proportional to the number density multiplied by the scattering cross section we can immediately calculate the ratio of the isotopic Raman cross sections, $\sigma_{14\text{-}15}/\sigma_{14\text{-}14} = 1.13 \pm 0.05$.

That this ratio differs from unity is not surprising. The expression for the Raman scattering cross section (Eq. (I.2) may be rewritten as

$$\sigma \propto \omega_i \omega_s^3 \left| \sum_{I,I_v} \langle B_v | I_v \rangle \langle I_v | A_v \rangle \langle B | r | I \rangle \langle I | r | A \rangle \left(\frac{1}{\Delta E_I} + \frac{1}{\Delta E_I'} \right) \right|^2 \qquad \text{(II.1)}$$

where ω_i is the incident frequency; ω_s is the scattered frequency;

A_v, B_v and I_v are the vibrational wavefunctions of the initial, final, and intermediate states, respectively; A, B, and I are the combined nuclear, rotational, and electronic wavefunctions of the initial, final, and intermediate states, respectively; and ΔE_I and $\Delta E_I'$ are resonant and antiresonant energy denominators associated with transitions to the intermediate state I. Consideration of only the difference in scattered frequencies between the isotopic molecules yields a value 1.01 for the isotopic cross section ratio. However, the differences in nuclear mass cause differences in the vibrational wavefunctions thereby causing differences in the Franck-Condon factors ($\langle B_v | I_v \rangle$ and $\langle I_v | A_v \rangle$) for different isotopic molecules. The Franck-Condon factors are of order unity and may be either positive or negative. Since the cross section is a coherent summation of contributions from a large number of intermediate states and the contribution from a single state can be shown to be of about the same magnitude as the total cross section, a considerable cancellation of contributions must occur. The differences in the Franck-Condon factors could therefore cause small differences in the isotopic cross sections, although direct calculation of these differences is not currently possible. Using the experimental value of $\sigma_{14\text{-}14} = 3.3 \pm 1.1 \times 10^{-31}$ $cm^2\text{-}sr^{-1}\text{-}mol^{-1}$ obtained by Fenner et al[12] we calculate a value for the cross section of $^{14}N^{15}N$, $\sigma_{14\text{-}15} = 3.7 \pm 1.4 \times 10^{-31}$ $cm^2\text{-}sr^{-1}\text{-}mol^{-1}$.

The studies in oxygen were performed using pure oxygen gas at 1atm. and 24°C. Otherwise, the experimental procedures were essentially the same as for nitrogen. Scans through the $^{16}O^{18}O$ and $^{16}O^{16}O$ Q-branches yielded the intensity ratio $I_{16\text{-}18}/I_{16\text{-}16} = 0.0043 \pm 0.0001$. Mass spectrometer analysis of the oxygen sample[24] yielded $N_{16\text{-}18}/N_{16\text{-}16} = 0.0041 \pm 0.0001$ from which a cross

section ratio of $\sigma_{16-18}/\sigma_{16-16} = 1.05 \pm 0.05$ was obtained. Using Fenner's value[12] for $\sigma_{16-16} = 4.3 \pm 1.4 \times 10^{-31}$ cm^2-sr^{-1}-mol^{-1}, the Raman cross section for $^{16}O^{18}O$ is computed to be $\sigma_{16-18} = 4.5 \pm 1.5 \times 10^{-31}$ cm^2-sr^{-1}-mol^{-1}. The results for both oxygen and nitrogen are summarized in Table VI. A further piece of useful information was obtained from this work. Namely, peak count rates of approximately 20 counts/sec were observed at both the $^{16}O^{18}O$ and $^{14}N^{15}N$ Q-branches.

Besides the preceding work, which has direct bearing on the isotope ratio measurements problem, we attempted to determine some of the molecular parameters of various isotopic nitrogen and oxygen molecules. As nitrogen and oxygen are symmetric diatomic molecules and thus infrared inactive, information on their fundamental parameters such as the rotational constant and equilibrium internuclear separation must be obtained by other means, e.g., Raman spectroscopy, M1 microwave spectroscopy, E2 absorption spectroscopy, or electronic absorption spectroscopy. One parameter, α_e, the rotation-vibration coupling coefficient, is important in determining the moment of inertia and equilibrium internuclear separation. Stoicheff determined α_e for $^{14}N^{14}N$ from electronic absorption data[14] while Bendtsen obtained a value for α_e by measuring the rotational constants in the ground and first excited vibrational states.[25] Weber and McGinnis determined α_e for $^{16}O^{16}O$ from the O- and S-branches of the rotation-vibration Raman spectrum.[15] However, by measuring the J-dependence of the Q-branch of the rotation-vibration Raman spectrum, α_e can be determined directly. Fletcher and Rayside used this technique to determine α_e for $^{16}O^{16}O$.[26]

The energy T of a vibrating diatomic rotor is given to second order by

$$T(v,J) = \omega_e (v + 1/2) + B_e J(J + 1) - \omega_e x_e (v + 1/2)^2 - D_e J^2(J + 1)^2 - \alpha_e J(J + 1)(v + 1/2) + \cdots \qquad \text{(III.2)}$$

TABLE VI

Isotopic Raman Scattering Cross Section Data

Nitrogen

I_{14-15}/I_{14-14}	0.0081 ± 0.0002
N_{14-15}/N_{14-14}	0.0072 ± 0.0001
$\sigma_{14-15}/\sigma_{14-14}$	1.13 ± 0.05
$\sigma_{14-14}(cm^2\text{-}sr^{-1}\text{-}mol^{-1})$	$3.3 \pm 1.1 \times 10^{-31}$
$\sigma_{14-15}(cm^2\text{-}sr^{-1}\text{-}mol^{-1})$	$3.7 \pm 1.4 \times 10^{-31}$

Oxygen

I_{16-18}/I_{16-16}	0.0043 ± 0.0001
N_{16-18}/N_{16-16}	0.0041 ± 0.0001
$\sigma_{16-18}/\sigma_{16-16}$	1.05 ± 0.05
$\sigma_{16-16}(cm^2\text{-}sr^{-1}\text{-}mol^{-1})$	$4.3 \pm 1.4 \times 10^{-31}$
$\sigma_{16-18}(cm^2\text{-}sr^{-1}\text{-}mol^{-1})$	$4.5 \pm 1.5 \times 10^{-31}$

where v and J are the vibrational and rotational quantum numbers, respectively, and the other quantities have their customary significance.[8a] The frequency $\bar{\nu}$ of lines in the Q-branch ($\Delta J = 0$, $\Delta v = 1$) is (to first order)

$$\bar{\nu} = T(v = 1, J) - T(v = 0, J) = \omega_e - 2\omega_e x_e - \alpha_e J(J + 1) \qquad \text{(III.3)}$$

Since $\omega_e - 2\omega_e x_e$ is a constant, by measuring the dependence of $\bar{\nu}$ (or any quantity related to $\bar{\nu}$ by an additive constant) on $J(J + 1)$, α_e can be determined directly.

Spectra were obtained on samples of natural oxygen gas, natural nitrogen gas, and 95% enriched ^{18}O gas at atmospheric pressure and 25°C. The Ar^+ laser was operated in a single axial mode at 488.0 nm with an output power of 700 mW. The $^{16}O^{16}O$ spectrum was taken at 0.14 cm^{-1} resolution, 1500 sec integration time, and ~0.05 cm^{-1} data point spacing; the $^{14}N^{14}N$ spectrum was taken at 0.14 cm^{-1} resolution, 1500 sec integration time, and ~0.03 cm^{-1} data point spacing; the $^{18}O^{18}O$ spectrum was taken at 0.12 cm^{-1} resolution, 1200 sec integration time, and ~0.05 cm^{-1} data point spacing. Wavelength determination was accomplished by interpolating between the initial and final readings on the wavelength vernier of the spectrometer. Previous calibration with spectral lamps indicated that when care was taken to avoid backlash problems, relative wavelength changes could be routinely measured to an accuracy of ±0.02 cm^{-1} over wavelength regions up to 200 cm^{-1} wide, although absolute wavelength measurements are restricted to accuracies of ±0.2 cm^{-1} (without simultaneous use of calibration lines) because of resetability limitations.

Figs. III-8 through III-10 show the spectra obtained by scanning through the Q-branches of the vibration-rotation Raman spectra of $^{16}O^{16}O$, $^{14}N^{14}N$, and $^{18}O^{18}O$, respectively, using the spectrometer settings described above. The centroids of the prominent lines in each spectrum were estimated and wavelength values and uncertainties assigned to each line by interpolation between the measured initial

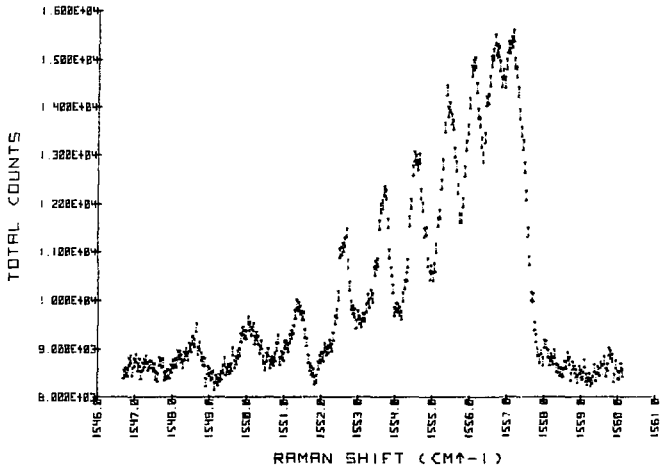

Fig. III-8. The Q-branch of the rotation-vibration Raman spectrum of $^{16}O^{16}O$.

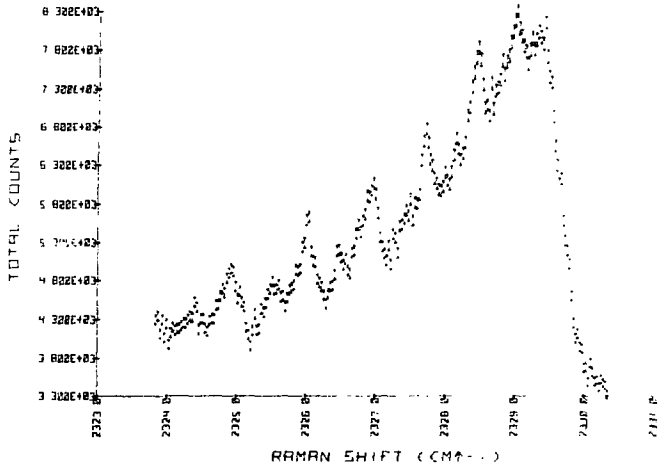

Fig. III-9. The Q-branch of the rotation-vibration Raman spectrum of $^{14}N^{14}N$.

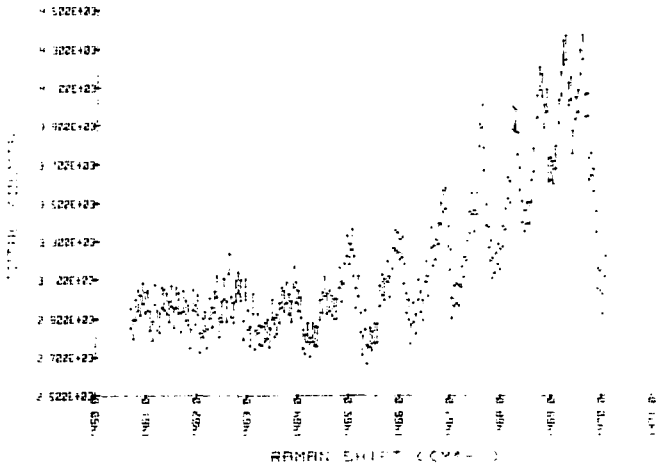

Fig. III-10. The Q-branch of the rotation-vibration Raman spectrum of $^{18}O^{18}O$.

and final wavelengths. J values were assigned to each line in the following manner. Taking the effects of nuclear spin into consideration (even-J levels are missing in $^{16}O^{16}O$ and $^{18}O^{18}O$ and odd-J levels have half intensity in $^{14}N^{14}N$) several trial estimates were made as to the correct J assignments. Using the calculated dependence of the intervals between the observed lines, the positions of the lines were extrapolated back to J = 0 or 1 (depending on the nuclear spin) for each trial. The J assignments corresponding to the trial which puts the J = 0 or 1 line closest to the observed position of the band edge were chosen for the determination of α_e. As the absolute wavelength of each line could not be accurately determined and addition of an arbitrary constant to Eq. (III.3) does not affect the J-dependence, only the wavelength difference between the start of the spectral scan and the position of each line was recorded. The J-assignments and wavelengths shifts of the observed lines are tabulated for all three isotopic molecules in Table VII.

For each isotopic molecule the wavelength shift was plotted versus J(J + 1) for all of the observed lines (Fig. III-11). Linear regression yielded the slopes ($= \alpha_e$) of these straight lines. An estimate of the standard error was obtained by repeating the linear regression with the first quarter of the points assigned maximum positive deviation, the middle half assigned no deviation, and the last quarter assigned maximum negative deviation. This analysis yielded the following results for α_e:

$^{16}O^{16}O$ $\quad \alpha_e = 0.01587 \pm 0.00010\ cm^{-1}$
$^{14}N^{14}N$ $\quad \alpha_e = 0.01736 \pm 0.00015\ cm^{-1}$
$^{18}O^{18}O$ $\quad \alpha_e = 0.01317 \pm 0.00010\ cm^{-1}$

The value for $^{16}O^{16}O$ is in excellent agreement with the experimental results of Fletcher and Rayside[26] ($\alpha_e = 0.01587 \pm 0.00035\ cm^{-1}$) and Babcock and Herzberg[27] ($\alpha_e = 0.015791 \pm$

TABLE VII

Summary of Experimental Data

$^{16}O^{16}O$	
J	Wavelength Shift (cm^{-1})
5	3.04 ± 0.03
7	3.41 ± 0.02
9	3.96 ± 0.02
11	4.62 ± 0.02
13	5.44 ± 0.02
15	6.32 ± 0.02
17	7.37 ± 0.02
19	8.56 ± 0.02
21	9.88 ± 0.02
23	11.30 ± 0.03
$^{14}N^{14}N$	
J	Wavelength Shift (cm^{-1})
4	0.97 ± 0.03
6	1.25 ± 0.02
8	1.78 ± 0.02
9	2.09 ± 0.02
10	2.48 ± 0.02
11	2.76 ± 0.02
12	3.27 ± 0.02
13	3.73 ± 0.02
14	4.19 ± 0.02
15	4.67 ± 0.02
16	5.33 ± 0.02
17	5.87 ± 0.03
$^{18}O^{18}O$	
J	Wavelength Shift (cm^{-1})
5	0.54 ± 0.02
7	0.89 ± 0.02
9	1.34 ± 0.02
11	1.86 ± 0.02
13	2.52 ± 0.02
15	3.25 ± 0.02
17	4.17 ± 0.02
19	5.07 ± 0.02
21	6.25 ± 0.02
23	7.43 ± 0.04

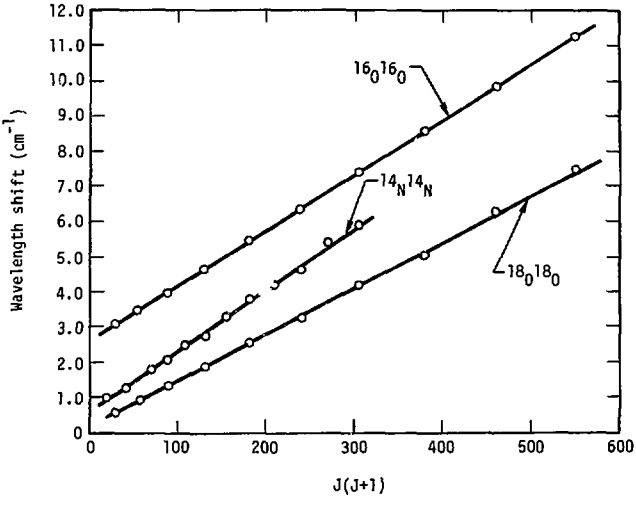

Fig. III-11. Plot of wavelength shift versus J(J+1) for lines in the Q-branches of $^{16}_{0}{}^{16}_{0}$, $^{14}_{N}{}^{14}_{N}$, and $^{18}_{0}{}^{18}_{0}$.

0.000010 cm^{-1}). Similarly, our result for $^{14}N^{14}N$ is in good agreement with the experimental results of Bendtsen[25] (α_e = 0.017292 ± 0.000003 cm^{-1}). There have been no previous determinations of α_e for $^{18}O^{18}O$. However, in the Born-Oppenheimer approximation, α_e for different isotopic molecules are related to their reduced masses μ through the expression[28]

$$\alpha_e' = (\mu/\mu')^{3/2}\ \alpha_e \qquad \text{(III.4)}$$

Using Eq. (III.4) and Babcock and Herzberg's value of α_e for $^{16}O^{16}O$, we obtain α_e = 0.013234 ± 0.000008 cm^{-1} for $^{18}O^{18}O$, which agrees well with our measured value. Similarly, using the value of α_e for $^{16}O^{16}O$ determined in this work, we obtain α_e = 0.01330 ± 0.00008 cm^{-1} for $^{18}O^{18}O$ which is also in agreement with our measured value.

Although microwave spectral measurements[29] have been made of some of the molecular parameters of $^{18}O^{18}O$, there have been no previous Raman spectra reported for this molecule (except our Q-branch spectrum). Consequently we decided to obtain complete rotational and rotation-vibration Raman spectra of $^{18}O^{18}O$ gas and to determine as many of its molecular parameters as possible. For this work the argon ion laser was operated multimode at 488.0 nm with approximately 1.2 W output power while the ratemeter - chart recorder system was utilized for recording the spectra. All spectra were obtained on a sample of 95%-enriched $^{18}O^{18}O$ gas at 1 atm and 25°C.

Several pure rotational Raman spectra were obtained at 0.3 and 0.5 cm^{-1} resolution, a scan rate of 120 cm^{-1}/hr, and an integration time of 3 sec. Also several rotation-vibration spectra were obtained at 0.5 and 1.0 cm^{-1} resolution, a scan rate of 30 cm^{-1}/hr, and an integration time of 30 sec. Frequent wavelength marks (determined from the spectrometer wavelength vernier) were recorded on each spectrum. Wavelength determination of the

lines in each spectrum was accomplished by interpolation betweer. these wavelength marks.

The pure rotational Raman spectrum of $^{18}O^{18}O$ is shown at 1 cm^{-1} resolution in Fig. III-12. A large number of low-intensity lines are observed interspersed among the high-intensity $^{18}O^{18}O$ rotational lines. These can be attributed to rotational lines from $^{16}O^{16}O$ and $^{14}N^{14}N$ impurities in the sample and to satellite lines induced by spin-spin and spin-rotation interactions[8a] in the $^3\Sigma_g^-$ ground state of $^{18}O^{18}O$.

Several pure rotational spectra were obtained at resolutions between 0.3 and 0.5 cm^{-1}. The centroid of each $^{18}O^{18}O$ line in these spectra was estimated and its wavelength determined by the interpolation procedure discussed above. As the $J \rightarrow J + 2$ Stokes and $J + 2 \rightarrow J$ anti-Stokes transitions are symmetric about the exciting line, the wavenumber differences between corresponding Stokes and anti-Stokes lines were computed and divided by two to yield the Raman shifts. The values of these shifts for each J from the different spectra were averaged to further minimize possible errors. These results are tabulated in Table VIII.

The Raman shift for a pure rotational line is given by [8a]

$$|\Delta\tilde{\nu}| = (4B_0 - 6D_0 + \ldots)(J + 3/2) - (8D_0 + \ldots)(J + 3/2)^2 + \ldots \quad \text{(III.5)}$$

The symbols have their customary meanings. Using polynomial regression to second order in J + 3/2 on the data in Table VIII yielded a value of D_0 which was more than an order of magnitude too large. This is not surprising considering that the magnitude of the second order term in Eq. (III.5) for J = 31 and a realistic value of $D_0 (< 10^{-5} cm^{-1})$ is less than the uncertainty in the positions of the lines. When the regression was performed to first order and neglecting D_0 ($6D_0 \ll 4B_0$), a reasonable value for B_0 was obtained,

$$B_0 = 1.2777 \pm 0.0012 \ cm^{-1}.$$

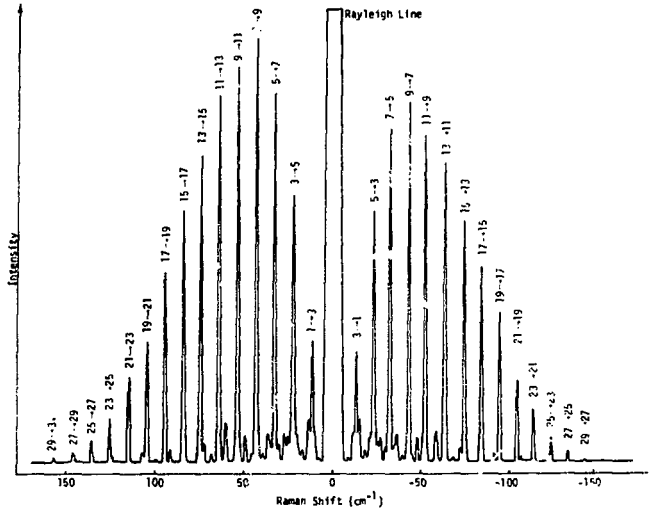

Fig. III-12. The pure rotational Raman spectrum of $^{18}O^{18}O$ (1.0 cm^{-1} resolution) showing the rotational quantum number assignments.

TABLE VIII

Raman Shifts for Observed Pure Rotational Lines in $^{18}O^{18}O$

J	Raman Shift (cm^{-1})
1	12.52 ± 0.10
3	22.77 ± 0.10
5	32.70 ± 0.10
7	43.42 ± 0.10
9	54.03 ± 0.10
11	64.47 ± 0.10
13	74.41 ± 0.10
15	84.78 ± 0.10
17	94.95 ± 0.10
19	105.08 ± 0.10
21	114.96 ± 0.10
23	125.28 ± 0.10
25	135.25 ± 0.10
27	145.75 ± 0.10
29	155.90 ± 0.10
31	165.57 ± 0.10

The uncertainty in B_0 was estimated from the uncertainties in each point by assigning the maximum positive deviation to the first quarter of the points, the maximum negative deviation to the last quarter, and no deviation to the middle half and repeating the regression.

Fig. III-13 shows the rotation-vibration Raman spectrum of $^{18}O^{18}O$ at 1.5 cm^{-1} resolution. The Q-branch ($\Delta J = 0$) of the $^{16}O^{16}O$ impurity is plainly visible between the $J = 17 \rightarrow J = 19$ and $J = 15 \rightarrow J = 17$ lines of $^{18}O^{18}O$. Several similar spectra were obtained at resolutions between 0.5 and 1.0 cm^{-1}. After determining the wavelengths of the Q-branch bandheads (of both $^{16}O^{16}O$ and $^{18}O^{18}O$), two sets of quantities were computed. The first of these is the wavenumber separation δ between the Q-branch bandheads. The second is one-half of the sum of the Raman shifts of the O-branch ($J+2 \rightarrow J$) and S-branch ($J \rightarrow J+2$) transitions, denoted $\Sigma/2$, corresponding to each value of J. As before the quantities determined from the different spectra are averaged and tabulated in Table IX.

The quantity $\Sigma/2$ is given by the expression

$$\Sigma/2 = -\alpha_e J(J + 3) + \Delta G_{1/2} - 3\alpha_e \qquad \text{(III.6)}$$

Polynomial regression of the $\Sigma/2$ values in Table IX to first order in $J(J + 3)$ yielded

$$\alpha_e = 0.01318 \pm 0.0027 \text{ cm}^{-1}$$

and

$$\Delta G_{1/2} = 1468.92 \pm 0.35 \text{ cm}^{-1}$$

From the bandheads we obtain

$$\delta = 87.31 \pm 0.60 \text{ cm}^{-1}$$

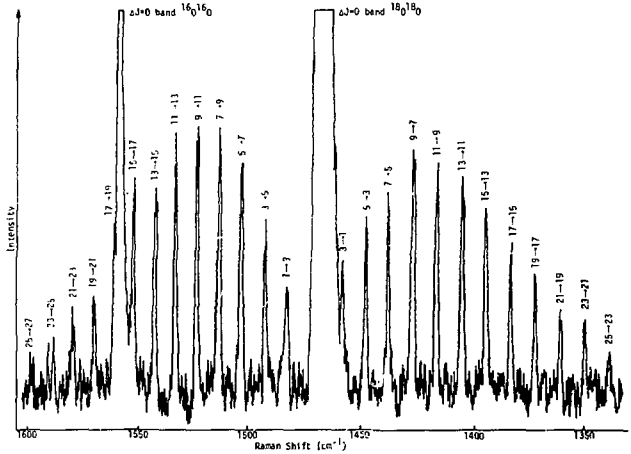

Fig. III-13. The rotation-vibration Raman spectrum of $^{18}O^{18}O$ (1.5 cm^{-1} resolution) showing the rotational quantum number assignments.

TABLE IX

Raman Shifts for Observed Rotation-Vibration Lines in $^{18}O^{18}O$

J	Raman Shift (cm^{-1})
1	1468.79 ± 0.20
3	1468.71 ± 0.20
5	1468.60 ± 0.20
7	1468.44 ± 0.20
9	1467.83 ± 0.20
11	1466.92 ± 0.20
13	1465.79 ± 0.20
15	1464.64 ± 0.20
17	1464.15 ± 0.20
19	1462.62 ± 0.20
21	1462.18 ± 0.20
23	1461.21 ± 0.20
25	1460.07 ± 0.20
27	1458.40 ± 0.20
Bandhead $^{16}O^{16}O$ Q-branch	1556.51 ± 0.30
Bandhead $^{18}O^{18}O$ Q-branch	1469.20 ± 0.30

Subtracting δ from the measured value of $\Delta G_{1/2}$ for $^{16}O^{16}O$ (= 1556.39 cm^{-1})[27] we obtain for $^{18}O^{18}O$

$$\Delta G_{1/2} = 1469.8 \pm 0.60 \text{ cm}^{-1}$$

in agreement with our prior measurement.

The equilibrium rotational constant B_e, moment of inertia I_e, and internuclear separation r_e are related to B_o and α_e through the relations

$$B_e = B_o + 1/2\alpha_e = \hbar/4\pi c\mu r_e^2 \qquad \text{(III.7)}$$

Using $\mu(^{18}O^{18}O) = 1.49442 \times 10^{-23}$g and our measured values of B_o and α_e we obtain

$$B_e = 1.2843 \pm 0.0013 \text{ cm}^{-1}$$

$$I_e = 2.1797 \pm 0.0022 \times 10^{-39} \text{g-cm}^2$$

and

$$r_e = 1.2077 \pm 0.0006 \times 10^{-8} \text{cm}$$

These results are tabulated in Table X along with data from other epxeriments and theoretical predictions.

As shown in Table X our values of B_o, B_e, I_e, and r_e are in good agreement with the microwave data of Steinbach and Gordy[29] while our value of α_e is in excellent agreement with the value obtained by direct resolution of the lines in the Q-branch of the Raman spectrum. The experimental values are also in good agreement with values predicted by considering the effects of differing isotopic masses[28] on the experimental values for $^{16}O^{16}O$ obtained by Babcock and Herzberg.[27]

TABLE X

Parameters of the $^{18}O^{18}O$ Molecule

Parameter	This Work	Other Experiments[Ref.]	Theory
$B_0(cm^{-1})$	1.2777 ± 0.0012	1.278008 ± 0.000001[29]	1.27842 ± 0.00001
$\alpha_e(cm^{-1})$	0.01318 ± 0.00027	0.01317 ± 0.00010 [Resolved Q-branch]	0.01323 ± 0.00001
$\Delta G_{1/2}(cm^{-1})$	1468.92 ± 0.35	---	1468.664 ± 0.001
$B_e(cm^{-1})$	1.2843 ± 0.0013	1.28484 ± 0.00021[29]	1.28504 ± 0.00001
$I_e(g\text{-}cm^2)$	$(2.1797 \pm 0.0022) \times 10^{-39}$	$(2.17870 \pm 0.00036) \times 10^{-39}$[29]	$(2.17788 \pm 0.00001) \times 10^{-39}$
$r_e(cm)$	$(1.2077 \pm 0.0006) \times 10^{-8}$	$(1.20743 \pm 0.00010) \times 10^{-8}$[29]	$(1.20740 \pm 0.00001) \times 10^{-8}$

Chapter IV: Isotope Ratio Measurements Using Raman Scattering

In the preceding chapters we have discussed the motivation for studying the use of Raman scattering as a tool for measuring stable isotope ratios, outlined some of the possible advantages and some of the possible problems of the technique, and presented Raman scattering data which is pertinent to the problem. In this chapter we discuss the Raman scattering isotope ratio measurement technique in more detail, outlining the mathematics of isotope ratio measurements, discussing possible systems for making these measurements, and making predictions of performance in a real system by extrapolating from the measured baseline data. We begin by discussing the mathematics of isotope ratio measurements.

Either an intensity (count rate) or a total number of counts may be measured by a photon-counting Raman spectrometer. The intensity, I_i, which is scattered from the i^{th} isotopic species and measured by a particular monochromator-detector system is given by

$$I_i = \epsilon_i' \sigma_i \rho_i L I_0 \qquad \text{(IV.1)}$$

where ϵ_i' is the detection efficiency of the monochromator-detector system for light scattered from the i^{th} species, σ_i and ρ_i are the Raman scattering cross section and number density, respectively, of the i^{th} species, L is the length of the scattering region, and I_0 is the incident laser flux (photons/sec). The measured number of total counts, N_i, is simply the time integral of I_i, which is given by

$$N_i = \epsilon_i' \sigma_i \rho_i L \int_{\tau_0}^{\tau_f} I_0 \, dt \qquad \text{(IV.2)}$$

when ρ_i is constant.

The fractional isotopic abundance, f_j, of an isotope j of element X is defined by the relation

$$f_j \equiv \frac{\sum_k n_{kj}\rho_k}{\sum_k n_{kX}\rho_k} \qquad \text{(IV.3)}$$

where n_{kj} is the number of atoms of isotope j in a molecule of species k and n_{kX} is the number of atoms of element X in a molecule of species k. The isotope ratio, R_{jk}, of isotopes i and j is defined by the relation

$$R_{ij} \equiv f_i/f_j \qquad \text{(IV.4)}$$

Substituting expressions for ρ_k obtained from Eqs. (IV.1) and (IV.2) into Eqs. (IV.3) and (IV.4) yields the expressions

$$f_j = \frac{\sum_k n_{kj} I_k \varepsilon_k^{-1}}{\sum_k n_{kX} I_k \varepsilon_k^{-1}} = \frac{\sum_k n_{kj} N_k \varepsilon_k^{-1}}{\sum_k n_{kX} N_k \varepsilon_k^{-1}} \qquad \text{(IV.5a,b)}$$

and

$$R_{ij} = \frac{\sum_k n_{ki} I_k \varepsilon_k^{-1}}{\sum_k n_{kj} I_k \varepsilon_k^{-1}} = \frac{\sum_k n_{ki} N_k \varepsilon_k^{-1}}{\sum_k n_{kj} N_k \varepsilon_k^{-1}} \qquad \text{(IV.6a,b)}$$

The expressions above are derived using the assumption that I_0 or $\int_{\tau_0}^{\tau_f} I_0\, dt$ are the same for all species k. The "effective efficiency" ε_k is defined by $\varepsilon_k^{-1} \equiv (\varepsilon_k' \sigma_k L)^{-1}$.

Since the n_{kj} and n_{kX} are easily determined numbers characteristic of the molecules being studied, the effective efficiencies, ε_k, for a system can be easily determined from Eqs. (IV.5a,b) or (IV.6a,b) by measuring the I_k or N_k for a sample whose f_j or R_{ij} have been accurately

measured by other means. Such a calibration would be necessary each time a different type of molecular system was used. Once the ϵ_k have been determined any number of f_j or R_{ij} measurements could be obtained with only occasional recalibration required.

These last results assume that the total laser flux (or total laser fluence) is the same for the intensity (or total counts) measurement of each isotopic species. One simple way of assuring that this is the case is by making all of the measurements simultaneously. Fig. IV-1 shows the prototype system for measuring isotope ratios using Raman scattering. The output of a high power cw visible laser (e.g. an argon ion laser) is directed into a cell containing the sample to be isotopically analyzed. Photons which are Raman scattered from the sample are collected and focused onto the entrance slits of a number of double monochromators each tuned to pass photons from the Q-branch of a different isotopic species. The number of monochromators required is determined by the number of isotopic species which must be included in the analysis. For example, only two monochromators are required to make 0.1% precision isotope ratio measurements in nitrogen ($^{14}N/^{15}N$), oxygen ($^{16}O/^{18}O$), or hydrogen ($^{1}H/^{2}H$) near natural abundance, while three monochromators are required to perform these same measurements on highly-enriched samples. The photons passed by each monochromator are detected by a photomultiplier tube whose output pulses are counted by the appropriate electronics. Using a system such as that of Fig. IV-1 isotope ratio measurements are made by simply counting photons simultaneously with each monochromator-detector system until the statistical uncertainties have been reduced to the desired level of precision and then inserting the measured values of N_m into Eqs. (IV.56) and (IV.6b).

For the preceding system to work properly, it is essential that the Q-branches of the various isotopic molecules be substantially

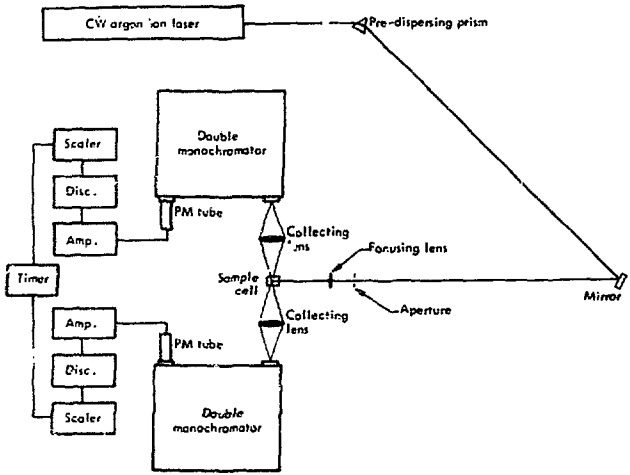

Fig. IV-1. Multi-monochromator system designed especially for isotope ratio measurements using Raman scattering.

free of interference from the spectral lines characterizing the other isotopic molecules. The spectral data presented in Chapter III indicate that cases of interest do exist where this is so. For example, Figs. III-3 and III-4 show that the Q-branches of $^{14}N^{15}N$ and $^{16}O^{18}O$ are free from interference from the rotational lines of $^{14}N^{14}N$ and $^{16}O^{16}O$, respectively. At natural abundance the intensities of the rotational lines of $^{14}N^{15}N$ and $^{16}O^{18}O$ are much less than 10^{-3} times the intensities of the Q-branches of $^{14}N^{14}N$ and $^{16}O^{16}O$, so the contributions of the rotational lines of the low-abundance species to the intensities of the high-abundance species may be neglected. Similarly, the concentrations of $^{15}N^{15}N$ and $^{18}O^{18}O$ are so much less than the concentrations of $^{14}N^{15}N$ and $^{16}O^{18}O$ that 0.1% precision measurements should be possible by measuring only the $^{14}N^{15}N/^{14}N^{14}N$ or $^{16}O^{18}O/^{16}O^{16}O$ intensity ratios.

Another important case is measurement of $^{16}O^{16}O/^{18}O^{18}O$ molecular isotopic ratios. Figs. III-6 and III-7 show that $^{16}O^{16}O$ and $^{18}O^{18}O$ are free of interference from each other. As a result it should be possible to measure $^{16}O^{16}O/^{18}O^{18}O$ molecular isotopic ratios to any reasonable precision at almost any relative abundance. This has specific significance in studies of isotopic fractionation. For example, Anbar and Heck have shown that if sufficiently accurate $^{18}O^{18}O/^{16}O^{16}O$ isotope measurements can be made, isotopic fractionation can be used to determine the mechanism for cooperativity in oxygen-hemoglobin binding.[30] It is doubtful that mass spectrometry can achieve the precision (approx. 1 part in 10^4) required for this study, whereas our Raman scattering technique should be able to achieve the required precision. Fig. III-5 shows that cases also exist which are not optimal for measuring isotope ratios using Raman scattering. Specifically, $^{16}O^{16}O$ does interfere with the Q-branch of $^{16}O^{17}O$. Thus, accurate $^{16}O/^{17}O$ isotope ratio measurements cannot be made without either reducing the amount of the $^{16}O^{17}O$ Q-branch which is collected (eliminating the $^{16}O^{16}O$ contribution but also

reducing the count rate) or complicating the data analysis to take account of the contribution from the $^{16}O^{16}O$ line to the count rate at the position of the $^{16}O^{17}O$ Q-branch.

Our photon-counting Raman spectrometer (Fig. II-2) is essentially one-half of the isotope ratio spectrometer shown in Fig. IV-1. As a result we may use the count rate data from the isotopic cross section measurements to determine by extrapolation the performance of a Raman scattering isotope ratio spectrometer. Peak count rates of approx. 20 counts/sec were obtained from the Q-branches of both $^{16}O^{18}O$ and $^{14}N^{15}N$ for an incident laser power of 1.3 W. Argon ion lasers are now available which can emit approx. 20 W at 488.0 nm. Thus using a double-pass scattering cell it should be possible to obtain 40 W of laser power. Extrapolating the count rate from the measured 20 counts/sec at 1.3 W we find 600 counts/sec at 40 W. Since a 0.1% precision isotope ratio measurement requires 10^6 counts from the low-abundance species, approx. 1700 sec or 30 min. are required to make such an $^{14}N/^{15}N$ or $^{16}O/^{18}O$ isotope ratio measurement at natural abundance using the extrapolated system. This is only a factor of two slower than the performance of a good mass spectrometer.

One way of improving the performance of the spectrometer system is by placing the sample inside the laser cavity (Fig. IV-2).[31] By replacing the output mirror of an Ar^+ laser with a maximum-reflectivity mirror the optical power inside the laser cavity (i.e. circulating between the mirrors) can be increased to many thousands of watts, as a consequence of the decrease in light losses. Although placing a scattering cell inside the laser cavity again increases these losses, optical powers exceeding 1000 watts can still be obtained from a laser with nominal 20 watts output power. Since the scattered intensity is directly proportional to the laser power, more than an order-of-magnitude increase in count rate could be obtained by using an intracavity scattering cell as compared to an

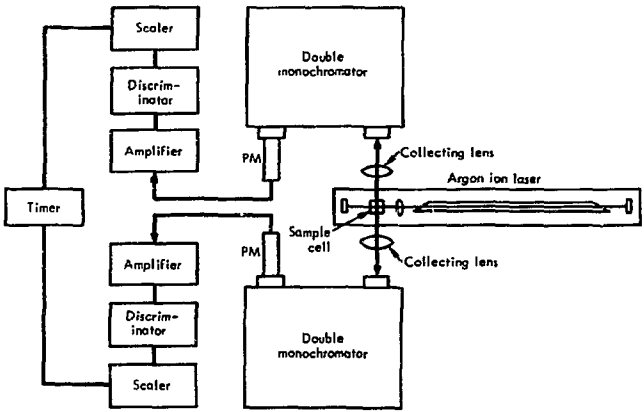

Fig. IV-2. Schematic diagram of a Raman-scattering isotope ratio spectrometer employing an intracavity scattering cell.

extracavity cell. This would result in over an order-of-magnitude reduction in the time required to make an isotope ratio measurement to any given precision. Assuming an intensity of 1000 W with the intracavity system we can extrapolate, as before, to a count rate of 15000 counts/sec. This means that only 70 sec are required to make 0.1% precision isotope ratio measurements in nitrogen and oxygen. This is an order-of-magnitude faster than any mass spectrometer can perform the same measurements. The intracavity cell approach does suffer the problem that the cell alignment in the laser beam becomes extremely critical as small changes in the cavity losses can cause large changes in the laser power. One solution to this problem is to design a method for transferring samples to and from the cell while it remains fixed solidly in the laser beam, a particularly attractive possibility in the case of gaseous samples.

Alignment of the sample with respect to the monochromators is also an important consideration. Small errors in sample placement can cause changes in the effective efficiencies of the monochromators which reflect themselves directly as errors in the isotopic ratios. The fixed cell mentioned above offers one solution to this problem. Another very attractive solution is to use a multichannel detector attached to a single monochromator so as to form a spectrograph, as shown in Fig. IV-3. Recent developments in detector technology have produced intensified silicon intensified target (ISIT) vidicon tubes which have approx. 10% quantum efficiency in the visible and almost unmeasurable noise (when cooled to $77^{o}K$)[32]. With appropriate electronics these vidicon tubes can be operated as 500-channel optical multichannel analyzers. In the system of Fig. IV-3 all isotopic species are analyzed at the same time with the same wavelength analyzer and the same detector. As a result errors in sample placement affect all of the effective efficiencies in the same relative manner and their changes divide out in Eqs. (IV.5) and (IV.6). Thus errors in sample placement affect the length of time required to make the measurements but not the accuracy of the measurements. Since each channel samples a different frequency,

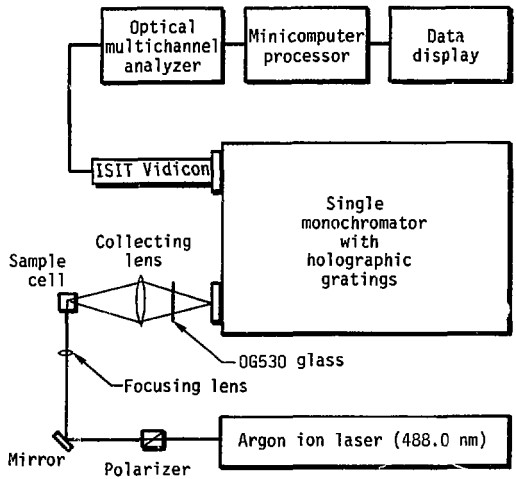

Fig. IV-3. Schematic diagram of a Raman-scattering isotope ratio spectrometer utilizing an optical multichannel analyzer.

in principle, up to 500 different isotopic species could be sampled with this system. In practice, a number of channels will be used for each Q-branch and a number will not be used at all, although it is definitely possible to make several different isotope ratio measurements simultaneously. If the output of the optical multichannel analyzer is connected to a minicomputer, direct digital output of the isotope ratios is possible, a very nice feature. The OG530 glass in Fig. IV-3 serves to reduce stray light problems. It has less than 10^{-6} transmission at 488.0 nm but passes more than 50% of the light scattered at wavelengths longer than 530.0 nm.

Another interesting idea concerns hydrogen-deuterium isotope ratio measurements. The isotope effect is so large in hydrogen that the Q-branches of the isotopic species $^1H^1H$, $^1H^2H$, and $^2H^2H$ are separated by many hundreds of wave-numbers. As a consequence it is not necessary to use monochromators to isolate the individual Q-branches; interference filters will suffice. A detector composed of an interference filter sandwiched between two f/1 lenses with a photomultiplier tube placed at the focus of one of the lenses and the scattering volume placed at the focus of the other lens can have an efficiency as high as 1% (i.e. an effective solid angle of 0.13 sr) for a photomultiplier tube with a quantum efficiency of 25%. Since a typical monochromator-detector system has an efficiency of 0.01% or less, a two order-of-magnitude increase in count rate is achieved by using interference filter detectors. Fig. IV-4 shows a system for measuring $^1H/^2H$ isotope ratios. Each of the three detectors has an interference filter whose peak transmission coincides with the Q-branch of a different isotopic species. If 488.0 nm laser light is used the filters should have their peak transmissions at 611.6 nm for $^1H^1H$, 592.6 nm for $^1H^2H$, and 571.2 nm for $^2H^2H$, each with 2.0 nm bandwidth. An extracavity cell arrangement is indicated in Fig. IV-4. This is because the increased efficiency of the interference filters yields

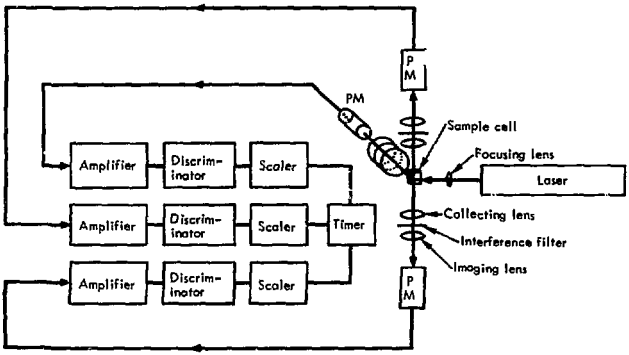

Fig. IV-4. Schematic diagram of a hydrogen-deuterium isotope ratio spectrometer.

high count rates without the inconvenience of using an intracavity scattering cell.

A somewhat exotic idea is to use the nuclear Raman effect[33,34] for measuring isotope ratios. The nuclear Raman effect is the inelastic scattering of gamma rays involving nuclear energy levels. Because of the nature of the strong interaction, different isotopes have vastly different energy levels, with resulting vastly different Raman shifts. Fig. IV-5 shows one possible system for utilizing the nuclear Raman effect. A beam of monochromatic gamma rays is generated by neutron capture in an appropriate target placed in a high-flux fission reactor. The scattered gamma rays are detected by a Ge(Li) detector coupled to a multi-channel analyzer. Analysis of the expected count rates indicates that this approach is not practical with currently available gamma ray beams (the photon fluxes being several orders of magnitude too low for even 1% precision measurements to be made in reasonable times). However, the nuclear Raman scattering approach should not be discarded entirely for two reasons. First, since only the nuclei are important, this approach could be used on solids, liquids, or gases and with any molecule or molecules. Second, possible advances in fission or fusion reactor technology or the advent of gamma ray lasers might make the requisite photon fluxes attainable.

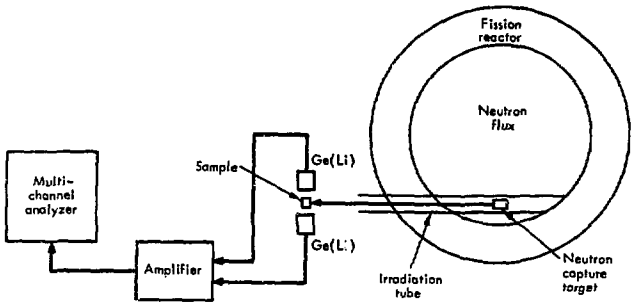

Fig. IV-5. Schematic diagram of an isotope ratio spectrometer system utilizing the nuclear Raman effect.

Chapter V: Conclusions

In this thesis we have described a number of studies aimed at evaluating the utility of Raman scattering as a technique for the rapid and precise measurement of isotope ratios and isotopic abundances. To accomplish these studies an unusual Raman spectrometer was constructed which utilized true photon-counting detection coupled to a completely automated data acquisition system. Incorporation of holographic diffraction gratings and a specially selected, cooled GaAs-photocathode photomultiplier tube yielded a spectrometer ideally suited to studying very weak Raman-scattered lines from gaseous samples.

Using this spectrometer the isotope structure of natural and enriched samples of nitrogen and oxygen gas was investigated. The resulting spectra indicated that the Q-branches of a number of isotopic molecules can be observed without interference from the rotational structure of the other isotopic molecules. The Raman scattering cross sections of $^{14}N^{15}N$ relative to $^{14}N^{14}N$ and $^{16}O^{18}O$ relative to $^{16}O^{16}O$ were measured and the cross section ratios were found to be different from unity, a fact which can be attributed to differences in the Franck-Condon factors of the different isotopic molecules. Resolution of the lines in the Q-branches of $^{16}O^{16}O$, $^{14}N^{14}N$, and $^{18}O^{18}O$ yielded direct measurements of the rotation-vibration coupling constants for these molecules. In addition, pure rotation and rotation-vibration Raman spectra were obtained for the first time from $^{18}O^{18}O$. Analysis of these spectra yielded good values for the molecular parameters of $^{18}O^{18}O$.

The theory pertinent to using Raman scattering for measuring isotope ratios was reviewed and a number of isotope ratio spectrometers have been examined. Calculations based on the experimental data indicate that $^{14}N/^{15}N$, $^{16}O/^{18}O$, and $^{16}O^{16}O/^{18}O^{18}O$ isotope ratios can be accurately measured by a properly-constructed Raman-scattering isotope ratio spectrometer over an order of magnitude faster than with a mass spectrometer. Consequently, it appears that Raman scattering promises to be a faster, more accurate, and non-destructive technique for measuring isotope ratios. It has a considerable potential impact on stable isotope tracer technology and may be of special utility as an on-line monitor of the output of isotope separation plants. However, there are two areas of research that

still need to be investigated as far as the Raman scattering isotope ratio measurements work is concerned. First, a full-scale isotope ratio spectrometer should be built and used to demonstrate the practical utility of this approach. Although the work described in this thesis has proved the feasibility of the approach, an application-prototype experiment has the obvious virtue of final demonstrability. Second, a conscientious effort must be made to determine the suitability for the technique of other candidate isotopes and molecular species. Of special interest are ^{13}C in CO_2 gas,[35,25] ^{33}S, ^{34}S, and ^{36}S in SO_2 gas,[37] ^{15}N in NO_3^- ions,[36] and ^{18}O 2,4-dinitrophenol (phenol-labelled) dissolved in nonpolar organic solvents.[38]

Acknowledgements

Foremost, I would like to express my deepest thanks to my thesis adviser, Professor Stewart D. Bloom, for his invaluable help with many portions of this research and for providing numerous intellectual diversions which have been of inestimable importance to my education. I would also like to express my thanks to Dr. Fred P. Milanovich, with whom I have collaborated in many areas of research (several of which are included in this thesis).

I would also like to thank Dr. Lowell L. Wood for his generous support of my various research projects and for many helpful discussions. Special thanks are due the Fannie and John Hertz Foundation for providing a fellowship during the last four years of my graduate studies.

I acknowledge the assistance and moral support of Professor Constant C. Delwiche and, on a sad note, the late Professor Emeritus Perry R. Stout, both of U. C. Davis, who were directly responsible for the instigation of this research. Prof. Stout passed away during the summer of 1975 only a few months before the completion of this work.

I would also like to express thanks to James L. Held and Donald J. Mullenhoff for assistance in assembling and maintaining the electronics used in the Raman spectrometer, Daniel W. Hansen and William L. Jackson for help with the mechanical construction of the spectrometer, and Mr. James E. Randolph for his help in obtaining some of the experimental data.

Finally, I owe an unpayable debt of gratitude to my wife, Jane, for putting up with me through five long years of graduate study.

References

1. R. E. Schreiber, "ICONS at LASL," Los Alamos Scientific Laboratory report LA-4759-MS (1971).
2. N. A. Matwiyoff, M. J. Reisfeld, T. R. Mills, B. B. McInteer, and M. Goldblatt, "The Stable Isotopes (ICONS) Research and Development Program at the Los Alamos Scientific Laboratory," Proceedings of the IAEA Symposium on Isotopes and Radiation Techniques in Studies of Soil Physics, Irrigation and Drainage in Relation to Crop Production, Vienna, Austria, Oct. 3-5, 1973.
3. N. A. Matwiyoff and D. G. Ott, Science, 181, 1125 (1973).
4. P. R. Stout, private communication (1975).
5. R. C. Harney and S. D. Bloom, "On the Feasibility of Isotopic Abundance Measurements Using Raman Scattering," Lawrence Livermore Laboratory report UCRL-51558 (1974).
6. S. D. Bloom, R. C. Harney, and F. P. Milanovich, Appl. Spectrosc., 30, 64 (1976).
7. R. C. Harney, S. D. Bloom, and F. P. Milanovich, ANAL, 170th ACS National Meeting, Chicago, Illinois, Aug. 24-29, 1975. Also Lawrence Livermore Laboratory report UCRL-76743 (1975).
8. Detailed discussions of the Raman effect in molecules may be found in:
   a) G. Herzberg, Spectra of Diatomic Molecules, Van Nostrand Reinhold 1950 and Infrared and Raman Spectra, Van Nostrand Reinhold 1945.
   b) A. Anderson, The Raman Effects, Vols. I and II., Marcel Dekker 1971.
   c) M. Tobin, Laser Raman Spectroscopy, John Wiley and Sons 1971.
9. W. Heitler, Quantum Theory of Radiation (3rd Ed.), Oxford Univ. Press.
10. W. Peticolas, Ann. Rev. Phys. Chem., 18, 233 (1967).
11. Y. Kato and H. Takuma, J. Opt. Soc. Amer., 61, 347 (1971).
12. W. R. Fenner, H. A. Hyatt, J. M. Kellam and S. P. S. Porto, J. Opt. Soc. Amer., 63, 73 (1973).

13. C. M. Penney, L. M. Goldman, and M. Lapp, Nature Physical Science, 235, 110 (1972).
14. B. Stoicheff, Can. J. Phys., 32, 630 (1954).
15. A. Weber and E. McGinnis, J. Mol. Spectrosc., 4, 195 (1960).
16. B. Stoicheff, Can. J. Phys. 36, 218 (1958).
17. The properties of monochromators employing holographic gratings are discussed in Handbook of Diffraction Gratings: Ruled and Holographic (1973). Available from Jobin-Yvon Optical Systems, 20 Highland Avenue, Metuchen, New Jersey, 08840.
18. An excellent discussion of photographic detection may be found in Kodak Plates and Films for Scientific Photography, Kodak Publication No. P-315 (1973). Available from Eastman Kodak Co., Rochester, New York 14650.
19. Diffraction Grating Handbook (1970). Available from Bausch and Lomb, Inc., Rochester, New York 14625.
20. Reference to a company or product name does not imply approval or recommendation of the product by the University of California or the U.S. Energy Research and Development Administration to the exclusion of others that may be suitable.
21. R. C. Harney and F. P. Milanovich, Rev. Sci. Instr., 46, 1047 (1975).
22. R. C. Harney and F. P. Milanovich, Automedica (in press).
23. D. N. Waters, SPEX Speaker, 20, #3, 7 (1975).
24. C. H. Otto, Lawrence Livermore Laboratory, private communications (1975).
25. J. Bendtsen, J. Raman Spectrosc., 2, 133 (1974).
26. W. H. Fletcher and J. S. Rayside, J. Raman Spectrosc., 2, 3 (1974).
27. H. D. Babcock and L. Herzberg, Astrophys. J., 108, 167 (1948).
28. H. H. Nielsen, Rev. Mod. Phys., 23, 90 (1951).
29. W. Steinbach and W. Gordy, Phys. Rev., 8A, 1753 (1973).
30. H. d'A. Heck and M. Anbar, Stanford Research Institute, private communication (1975.
31. L. L. Wood, Lawrence Livermore Laboratory, private communication (1975).

32. The properties of vidicon detectors are discussed in OMA Catalog (1975). Available from Princeton Applied Research Corp., Princeton, New Jersey 08540.
33. Z. Maric and P. Mobius, Nucl. Phys., 10, 135 (1959).
34. H. E. Jackson, G. E. Thomas, and K. J. Wetzel, Phys. Rev., C9, 1153 (1974).
35. J. Flores, I. Koenig, and W. Bonner, NASA Ames Research Center, private communication (1975).
36. P. Stout (deceased) and C. C. Delwiche, Univ. of California, Davis, private communication (1975).
37. J. Shinn, Lawrence Livermore Laboratory, private communication (1975).
38. J. Kirsch, University of California, Berkeley, private communication (1975).